

Answers to the referee comments

We thank all referees for the valuable and constructive comments. We have addressed all the points one-by-one as listed below. The page/line numbers indicating the changes in the replies are given with respect to the old manuscript, and may differ from the modified one. The manuscript is revised accordingly, with all changes marked using the latexdiff program, and is included in this document after the replies.

Referee #1

1. Cross comparisons with other data sets are very important. This reviewer found that the O profile of 20-30N, Apr., 2004 in Figure 13 is very consistent with the results of Xu et al., [2012] (see Figure 5). Figures 5 and 6 in Xu et al., [2012] show that the retrieved O profiles at north hemisphere, south hemisphere and equator are very different, which dependent on seasons. How about GOMOS measurements? The comparison and discussions should be added.

According to the referee's comment, we added the following comparison similar to Xu et al. (2012) (see Fig. 5&6). The plot below provides the comparison of derived GOMOS atomic oxygen profiles, at 30°-50°N, 10°S-10°N and 30°-50°S for (a) Mar. and (b) Jul. 2003, respectively.

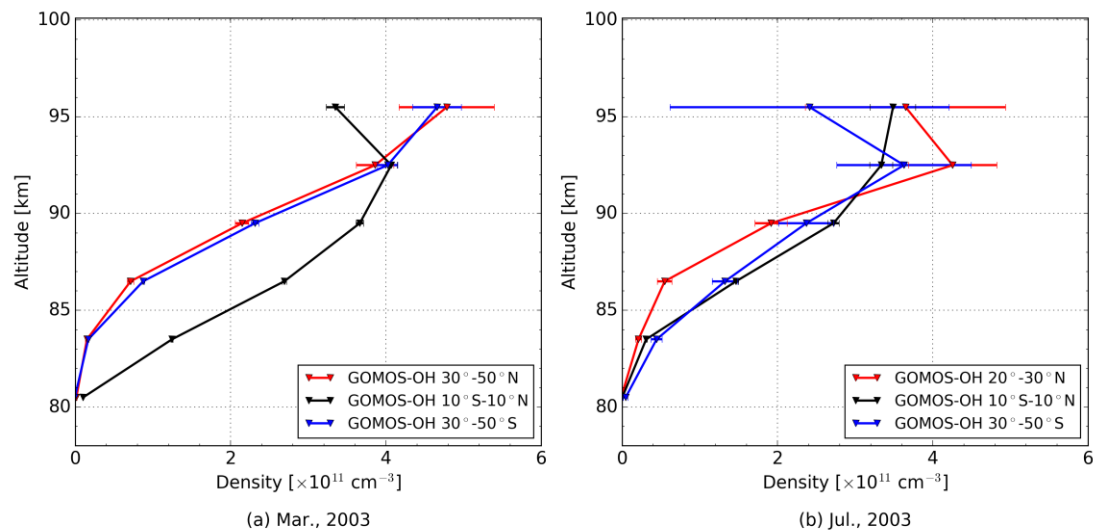


Figure. The Comparison of derived GOMOS atomic oxygen profiles, at 30° -50° Jul. 2003, respectively. Since the data for 30° -50° N, Jul. 2003 is not available in GOMOS, it is substituted by the data from 20° -30° N of this month.

This figure provides the comparison among the derived GOMOS atomic oxygen profiles from the equator, the northern and southern hemispheres, for both the spring equinox (Mar.) and summer solstice (Jul.) seasons. In March, the atomic oxygen abundances at the equator are larger than those at both hemispheres below 92 km, but above they become smaller than the northern and southern hemisphere values. However, in July, the atomic oxygen density is found to be largest in the northern hemisphere above 91 km. The data from Xu et al. (2012, see Fig. 5&6) also shows a similar behaviour, despite of the larger absolute values, which may be due to the larger radiance as measured by SABER.

2. P2 L1-2: “although it is difficult to obtain a consistent global picture of absolute density values from these measurements, which differ by a factor of more than 40” What are values of the

absolute density from these measurements? How about the local time and locations of these measurements?

Offermann et al., [1981] (see Tab.6 and Fig.7) reviewed the rocket experiments prior to 1980 and summarized the corresponding absolute atomic oxygen density measurements. These measurements were obtained by three kinds of measurement technology, which provide data differing by one order of magnitude. The highest values are delivered by the mass spectrometers with a cryo-ion source, which are $5.8\sim 9.8\times 10^{11}\text{cm}^{-3}$ at peak height, and those measurements were taken at $37\sim 40^\circ\text{N}$ latitude, at local time of 23:31, 01:25, 20:16 and 15:30. The second group is given by the technique of ultraviolet absorption and resonant scattering, the absolute value of which are about $7.8\sim 28\times 10^{11}\text{cm}^{-3}$ at peak height. The location of the experiments is at 57°N latitude, and the local time scatters around noon (11:04, 12:56, 13:59) and midnight (22:37, 23:09, 23:55). The last group are provided by the cryo-pumped mass spectrometer, and their values vary around $0.87\sim 9.1\times 10^{11}\text{cm}^{-3}$ at peak height. They are obtained at $30\sim 38^\circ\text{N}$ latitude, with local time in the afternoon (14:30, 14:32) and near midnight (22:23, 22:33, 22:34, 02:16).

All the measurements were measured in the mid-latitudes of the north hemisphere, and the local time is either near the noon or at the midnight. However the obtained atomic oxygen values diverge by more than one order of magnitude, and even for the same measuring technique, the values are variable. Therefore, Sharp, [1991] concluded it to be “differ over a factor of 40”.

We added “Offermann et al., [1981]” also in the reference list for this sentence.

3. P2 L35: “GOMOS”→“GOMOS (Global Ozone Monitoring by Occultation of Stars)”.

We modified the text according to the referee’s comment.

4. P9: Do these errors relate to latitudes?

Generally, we do not see a significant latitude dependence of the errors of the derived atomic oxygen from GOMOS measurements.

5. P10 L4-6: “migrating diurnal tides, which have a maximum wind amplitude over the equator and two weaker maxima of opposite signs at mid-latitudes.” Which component of wind? Zonal or meridional wind or vertical wind? How about the peak height of the migrating tides in wind? This might be the fundamental for the downward and/or upward displacement of [O]. Please clarify the procedure.

As the local time of the GOMOS observation is limited to midnight, it is difficult to deduce migrating diurnal tides from the GOMOS atomic oxygen dataset. Besides, the nonmigrating diurnal tides could also influence the spatial distribution of atomic oxygen and OH emissions (Xu et al. 2010). Therefore, it is difficult to characterize migrating tides as provided by GOMOS.

According to the referee’s comment, to clarify the procedure, we modified the sentences in P10, Line 4 as follows:

“As already mentioned and discussed by Smith et al. (2010) and Xu et al. (2010), the latitudinal distribution structure of atomic oxygen is influenced by tides. The vertical transport of air caused by tides leads to a vertical displacement of atomic oxygen.”

6. P10: Equation (1), What is the physical meaning of “Offset”?

According to the referee’s comment, we modified “offset” to “baseline”, and added the following sentence in P11 Line 6 to describe its physical meaning:

“The baseline is given as the averaged value of the monthly mean column densities along the time series.”

7. P12 L6-7: “18%” and “9.6%”, How about the baseline of this percentage?

All the percentages, 17.1%, 18%, 9.6% and 1.7% are calculated with respect to the baseline value.

According to the referee’s comment, we modified the text in P12 Line 6: “the amplitude is about 18% (with respect to the baseline)”

Referee #2

General point:

In my opinion, the introductory material focuses too much on the level 1 data and not nearly enough on the retrieval (level 1 to level 2) process. It might not be necessary to cut text about the level 1 data, but much more detail about the retrieval algorithm itself is needed, e.g. what kind of retrieval algorithm is it (as Rogers outlines many different schemes)? What did you use for your a priori?

Our retrieval approach is based on the Gauss-Newton iteration scheme, with the zero- and first- order Tikhonov regularization matrix applied. The a priori data about the absolute value of atomic oxygen is taken from MSIS model, and is averaged into the vertical grid of 3 km as the measurements for the zero-order matrix, and the first-order derivative matrix for smoothing is constructed from the linear gradient of two consecutive atmospheric layers. We modified the paragraph in P7, Line 10-17 to clarify it:

“The inverse model applies a constrained global-fit approach following the formalism of Rodgers (2000). The Gauss-Newton iterative method in the n-form (Rodgers, 2000, p. 85) is chosen to minimize the cost function of this inverse problem. Besides, a priori information about the atmospheric state is included in the retrieval for regularization to mitigate the influence of measurement errors. The a priori information about atomic oxygen in this work is taken from MSIS model data, and the zero- and first- order Tikhonov regularization matrices (Tikhonov and Arsenin, 1977) are considered in the cost function. The a priori data about the absolute value of atomic oxygen is taken from MSIS model, which is averaged into the vertical grid of 3 km as the measurements. The first order regularization is obtained from the linear interpolation of the a priori data given on the measurement grid, i.e., no sub measurement-grid information is obtained from that data. The regularization strength depends on altitude and its main purpose is to assure meaningful values at the upper and lower boundaries of the altitude regime considered. In between, the regularization has virtually no effect on the retrieved quantities, as can be seen from the retrieval diagnostics. The vertical resolution of the retrieval results are close to the vertical grid of the measurements. The target parameters of the retrieval are the vertical profiles of atomic oxygen abundance, spectral resolution, and a wavelength shift. The latter are both altitude-independent and give a better agreement between measured and simulated spectra. The content of information in the spectra is sufficient to retrieve these additional parameters.”

What assumptions are made in the forward model that could lead to potential uncertainties in the L2 data?

The assumptions in the forward model that could lead to potential uncertainties in the L2 data, are mainly forward model parameters (the reaction and quenching rate coefficients, Einstein coefficients) and the atmospheric background input profiles (temperature, ozone, density).

Specific points:

1. P1 Line 3: “based on” should be “derived from”.

We modified the text according to the referee’s comment.

2. Line 22: there should be “e.g.” at the start of the reference list.

We added “e.g.” in the text according to the referee’s comment.

3. P3 Line 2: OH($v=8$) should be OH(8-4).

We modified the text according to the referee’s comment.

4. Line 12: please change “entities” to some thing like trace species, or atmospheric states.

We modified “entities” to “trace species and temperature profiles” according to the referee’s comment.

Also, what is meant by “mostly”?

Besides the stellar transmission measurements, the GOMOS instrument is equipped with two photometers, which deliver the stellar flux radiance measurements. Since the word “mostly” here is unclear, it is deleted in the text.

5. Line 14: “descending node equator crossing time” is redundant.

We changed “descending node equator crossing time” to “equator crossing time (descending node)” according to the referee’s comment.

6. Line 23: “lights” should be “emissions”.

We modified the text according to the referee’s comment.

7. P4 Line 19: please, briefly, explain “star leakage” in the text.

We added the following sentences in the text according to the referee’s comment.

“The star is a point source, and part of the stellar light is spread to the lower and upper band, which is supposed to be totally imaged in the central band in an ideal case.”

8. P5 Line 12: what is meant by “quantified”?

We rephrased the sentence to “the quality of the reprocessed spectra are evaluated” in the text to make it clear.

9. P6 Fig 3: “altitude” should be either “tangent altitude” or “tangent height”.

We changed “altitude” to “tangent altitude” in the caption according to the referee’s comment.

10. Fig 4: If I’m understanding this correctly you’re showing slant column radiances, in which case it should really be “tangent height” (this would also need to be corrected in the caption and anywhere else it is discussed).

According to the referee's comment, we changed:

The caption and the label of the right plot in Fig.4: "altitude" to "tangent altitude".

P5 Line 16: "at around 85 km" to "at the tangent altitude of around 85 km".

The caption and the label of the right plot in Fig.5: "altitude" to "tangent altitude".

The caption in Fig.11: "altitude" to "tangent altitude".

The caption and the label of the right plot in Fig.12: "altitude" to "tangent altitude".

11. P7 Line 10: there are many approaches given in Rogers. As your technique hasn't been published before, you need to have a lot more detail here about the retrieval algorithm.

According to the referee's comment, we added the following sentence in P7 Line 10:

"The Gauss-Newton iterative method in the n-form (Rodgers, 2000, p. 85) is chosen to minimize the cost function of this inverse problem."

12. Line 11: it is unclear what "complemented by variables" means. As it is, it sounds like the intention is to retrieve, e.g., wavelength shift parameters. Are you retrieving those? Or are you just trying to say that there is a wavelength shift taken into account in the spectral fitting?

The variables for the spectral resolution and wavelength shift are also simultaneously derived as the atomic oxygen abundances.

According to the referee's comment, we modified the sentence in P7 Line 11 for clarity as:

"The target parameters of the retrieval are the vertical profiles of atomic oxygen abundance, spectral resolution, and a wavelength shift. The latter are both altitude-independent."

13. Line 15: where is your a priori coming from? If you say that it's coming from the "real atmosphere" that implies that you already know what the true state is. Your a priori needs to be described in much more detail.

According to the referee's comment, we modified the last paragraph of P7:

"Besides, a priori information about the atmospheric state is included in the retrieval for regularization to mitigate the influence of measurement errors. The a priori information about atomic oxygen in this work is taken from MSIS model data, and the zero- and first- order Tikhonov regularization matrices (Tikhonov and Arsenin, 1977) are considered in the cost function. The a priori data about the absolute value of atomic oxygen is taken from MSIS model, which is averaged into the vertical grid of 3 km as the measurements. The first order regularization is obtained from the linear interpolation of the a priori data given on the measurement grid, i.e., no sub measurement-grid information is obtained from that data. The regularization strength depends on altitude and its main purpose is to assure meaningful values at the upper and lower boundaries of the altitude regime considered. In between, the regularization has virtually no effect on the retrieved quantities, as can be seen from the retrieval diagnostics."

14. P8 Line 3: "longtime" should be "time"

We modified the text according to the referee's comment.

15. Fig 5 (right): I get somewhat nervous when I see measured and fitted profiles that agree that well. How did you choose to show this specific profile? Is this a typical fit, or is it one of the best fits? Some discussion needs to go in to why this example was chosen.

The shown plot is considered to be one of the best fit results, that the total radiance of the raw and the fit are nearly identical. We chose to show the plot here with the intention to illustrate what a best fitting case is like.

According to the referee's comment, we changed this sentence in P8, Line 4, and provided a plot showing a typical fit: "Shown in Figure 5 (left) is a typical profile of the fitted spectra compared with the measurements. In general, simulations and measurements are in good agreement. The spectrally integrated radiance in Figure 5 (right) also show consistency."

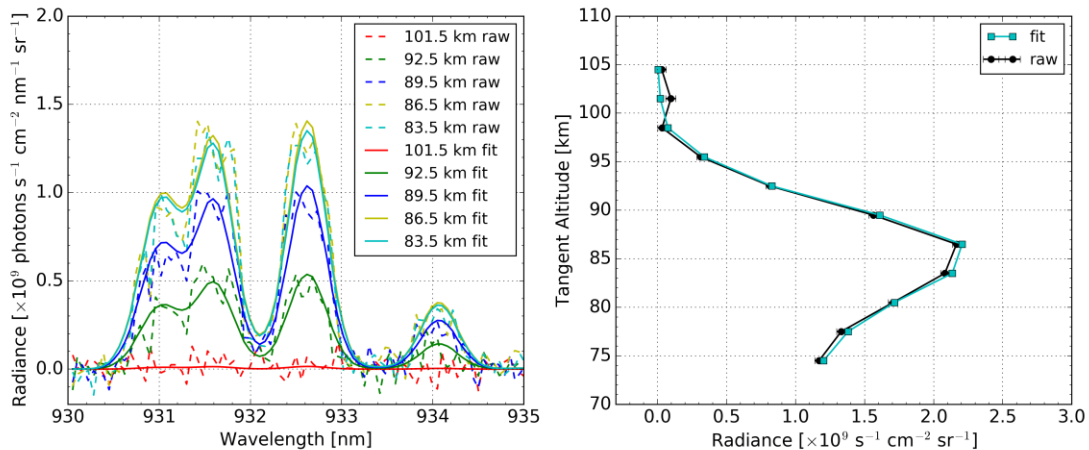


Figure 5. (Left) Simulated spectra (fit, solid line) and measurements (raw, dashed line) of GOMOS monthly zonal mean measurements of OH(8-4) airglow emissions at tangent altitudes, as given in the figure legend for Aug. 2003 at 30°–40° S and a local time of 10–12 p.m.. (Right) The spectrally integrated radiance over 930–935 nm versus tangent altitude for the same conditions.

Also, the y-axis is labelled as “altitude”. Again, if I’m understanding this correctly you’re showing slant column radiances, in which case it should really be “tangent height” (also needs to be corrected in the caption).

We changed “altitude” to “tangent altitude” in the plot and the caption according to the referee’s comment.

16. Line 15: “accuracy” is probably not the correct term here (implies systematic error). I think you’re discussing “total uncertainty”.

We changed “accuracy” to “total uncertainty” according to the referee’s comment.

17. P9 Fig 6 caption: “lower” should be “lesser”.

We modified the text according to the referee’s comment.

18. Lines 1-10: this section just needs a few lines of text describing how the error estimates were calculated (presumably through error propagation).

According to the referee’s comment, to describe the error estimation process, we added the following sentences in P8 Line 17:

“The influence of these uncertainties on the results are assessed through error propagation, by the perturbation of forward model parameters.”

And in P9 Line 8 we added in the sentence: “Through error propagation calculation”.

19. Multiple instances: “average kernel” should be “averaging kernel”.

According to the referee’s comment, we changed “average kernel” to “averaging kernel” in the caption of Fig.7, P9 Line 13, Line 14 and Line 16.

20. Lines 17-18: it is not the fact that the vertical resolution is close to the retrieval grid that tells you that the results is coming from the measurements and not the a priori. That information comes from the sum of the averaging kernels (which you have plotted and is near 1). Please discuss this.

According to the referee’s comment, we modified the sentences in lines16-18 to explain the vertical resolution of the retrieval:

“and the corresponding vertical resolution for each altitude is around 3 km, which is close to the vertical spacing of the limb measurements. Since the sum of the averaging kernels is also near one, the a priori influence is generally low.”

21. P10 Fig 7 caption: “The retrieval altitude grid refers to the vertical resolution of the derived quantities”. It’s unclear what you were trying to say here.

According to the referee’s comment, for clarity we changed the label in the right plot of Fig.7 to “vertical resolution” and also rephrased the caption:

“The vertical resolution is obtained from the distribution of each row in the averaging kernel by calculating the corresponding FWHM.”

22. Eq 1: It may not be strictly necessary, but why are you only fitting to an offset and not an offset + slope? I assume the slope wouldn’t be significant, but it would be nice to have for completeness.

According to the referee’s comment, a slope term is added in the linear fit component for the harmonic analysis, and the fitting result is shown below in the figure and discussed below:

“The agreement between measurements and the fit increases marginally by about 2% with an additional slope term. But the fitting parameters are not independent any longer, because a strong correlation between the slope, the baseline and the solar terms are found (see Figure below), which was not the case before. This indicates that the inversion problem (to obtain the fitting parameters) is now under-determined.

As an alternative approach, the solar (F10.7) fitting parameter could be replaced by the slope term. In this case, the residual increases by about 5% and the fitting parameters are not correlated (except for the offset and slope terms). From a mathematical point of view, this is an alternative to the original fit (with solar, but without slope terms). For this setup, the slope is $-0.0002 \times 10^{12} \text{ cm}^{-3} \text{ month}^{-1}$, which means that there is virtually no trend apparent in the data.

This can be explained, if the change over time is considered as a combination of two linear trends, with a negative slope in the declining phase of the solar cycle and a positive slope in the following inclining phase. This hypothesis can be underpinned by looking at a subset of the time series, covering the time period from 2002 to 2009, only (roughly solar maximum to solar minimum). The slope for this period is about -3% per year, indicating a linear decrease of atomic oxygen by 21% for the given period. If the F10.7 dependency is considered instead, a similar drop is modeled, if a solar term with an amplitude of $0.0025 \times 10^{12} \text{ cm}^{-3} \text{ sfu}^{-1}$ is used.

This value is similar to $0.002 \times 10^{12} \text{ cm}^{-3} \text{ sfu}^{-1}$, which is the value obtained when the total time series is considered.

To the authors' opinion, this line of arguments indicates that there is more likely a solar F10.7 dependency apparent in the data than a plain linear dependency."

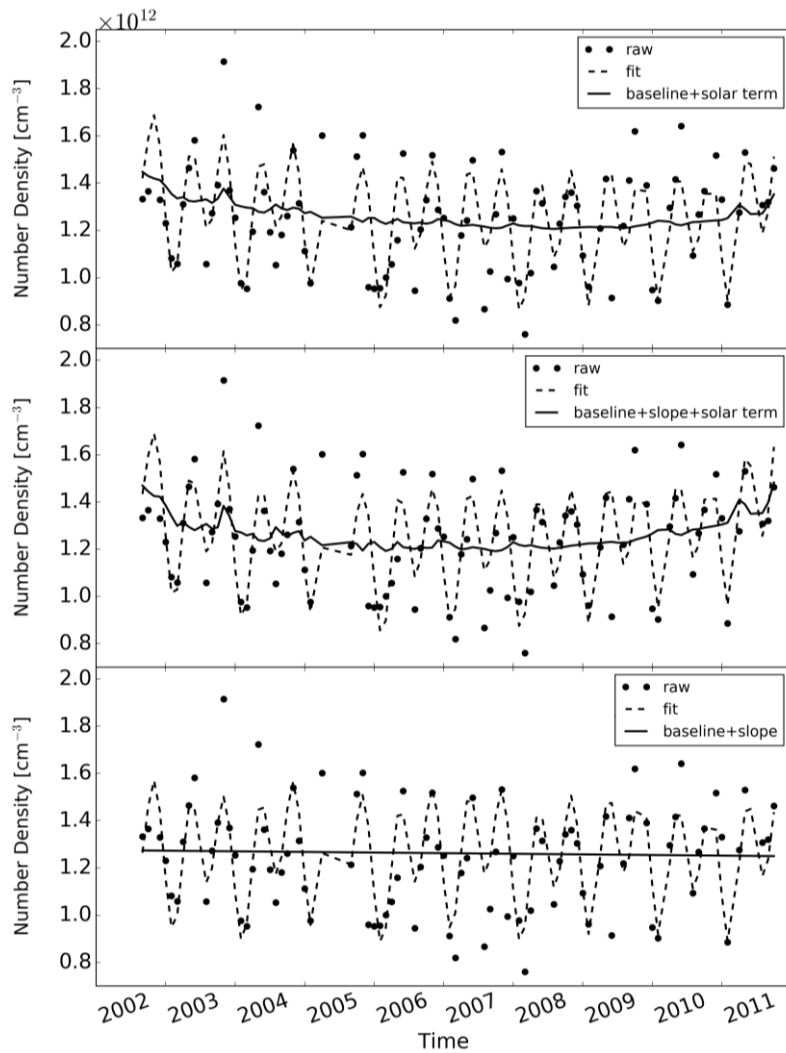


Figure. Multiple linear regression analysis of vertically integrated, monthly mean atomic oxygen densities of 80–97 km for 20°–30° N from 2002 to 2011. (first panel) The raw and fitted data are shown. The fitting is obtained by considering the baseline, the solar term, SAO, AO and QBO terms in the harmonic analysis. The baseline plus the solar term is given additionally. (second) A slope term is included in the fitting along with the solar term. (third) The solar term is replaced by a slope.

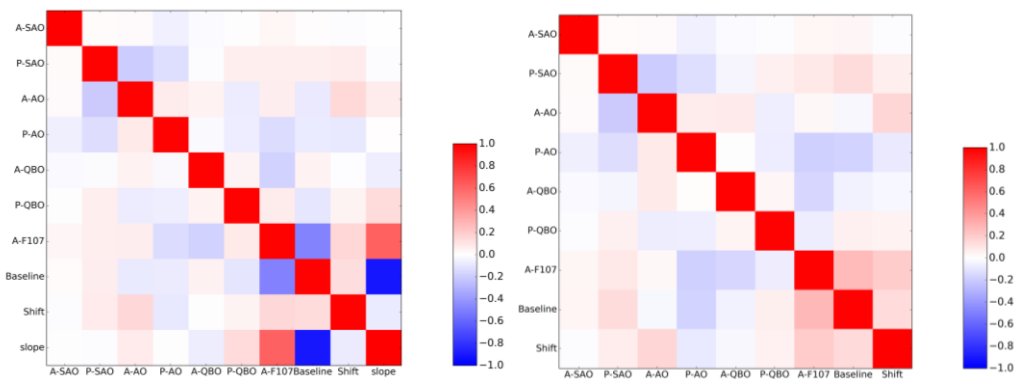


Figure. The correlation matrix (left) with and (right) without the slope term for full data series

According to the referee's comment, we added the above description at the end of section 4.3.

23. P11 Lines 9-10: Please rephrase this sentence, as it doesn't fully or accurately define what is being shown in Fig 10.

According to the referee's comment, we rephrased this sentence to describe the Fig.10:

"In Figure 10, the raw data and the fitting results are illustrated in the upper panel. Besides, the baseline plus the solar terms are also shown in the plot. The SolarMin and SolarMax values denote the fitted atomic oxygen column densities solely from the solar cycle component, under the solar minimum and solar maximum conditions respectively. The SAO and AO components from the harmonic fitting are given in the middle and lower panel respectively."

24. P12 Fig 9 caption: could be good to remind people that the time bins are monthly means.

We changed the caption to "Temporal evolution of the vertical distribution of monthly zonal mean atomic oxygen densities" according to the referee's comment.

25. Line 1: I could easily be wrong, but I doubt that the uncertainty on the solar cycle fit is precise to 0.1%. If it is, fine. But if not, I'd recommend rounding 17.1% to 17% (same with 9.6% at line 7).

According to the referee's comment, the precision of the fitting results was reconsidered. We rounded up the numbers for the solar cycle, AO and QBO fit components.

P12 Line 1 & Line 3: 17.1% to 17%.

P12 Line 7: 9.6% to 10%.

P12 Line 9: 1.7% to 2%.

26. P13 Fig 10: the AO and SAO panels are missing units (relative amplitude, I assume), same for the given P values (months, I assume).

According to the referee's comment, we modified Fig. 10 to include the units of SAO and AO panels, which is the amplitude, and also the P values. We also added in the caption: "The phase shifts are in unit of months."

27. Fig 10 and Table 2: It is unclear what the values for Solar Max and Solar Min represent. Please explain in the text and captions.

According to the referee's comment, we added in the text and the captions the explanations about the SolarMin and SolarMax:

"The SolarMin and SolarMax values denote the fitted atomic oxygen column densities solely from the solar cycle component, under the solar minimum and solar maximum conditions respectively."

28. P14 Line 1: This may be a matter of opinion, but "validation" requires in depth analysis of comparisons with multiple other instruments. I would recommend changing the name of this section to "comparisons with SCIAMACHY".

We changed "validation by" to "comparison with" according to the referee's comment.

29. Line 9: Did SCIA “always” measure at 10PM? Surely, that must change somewhat with latitude? Perhaps “always measured near 10pm”?

The SCIAMACHY instrument do not “always” measure at 10 p.m. but around 10 p.m.. SCIAMACHY recorded a swath of 960 km in horizontal direction and covered local times mostly between 21:00 and 23:00 at tangent points. Besides, the local time varies gradually to an earlier/later time with increasing latitude. We modified the sentence to “always measured near 10 p.m.” to make it accurate.

30. Line 17: could perhaps also mention fields-of-view.

We added “fields-of-view” into this sentence according to the referee’s comment.

31. Line 27: Please clarify what you mean by “consistent”. Do you mean agree within the combined uncertainties?

We changed the sentence to “agree with each other within the combined uncertainties” in the text to make it clear.

32. Lines 32-33 (and on next page): When you use “OH(v=8) emissions”, it makes me think that you’re measuring multiple OH(v=8) bands, when I believe you’re only looking at 8-4 (same with the v=9 instances). Please use the more specific notation. Also, at some point early on you should define that OH(8-4) means OH(v=8 -> v=4).

According to the referee’s comment, we changed the notation in these sentences from “OH(v=8)” to “OH(8-4)” and “OH(v=9)” to “OH(9-6)”. Besides, we added the definition of OH(8-4) in P5 Line 10: “It includes a number of emission lines from OH(v=8-4) band, which originates from the radiative transitions of OH(v=8-v)=4.”

33. P15 Fig 11: One thing that immediately grabs your attention in this plot is that the difference is becoming noticeably more positive over time, which seems to indicate that there’s a drift in one, or both, of the data sets. Can you please comment in the text what might be the source of this change over time?

According to the referee’s comment, we added in the text (P14 Line 19) to explain the potential source of this change: “Particularly, the difference of the GOMOS data to the SCIAMACHY data is gradually becoming positive from negative over time, and the potential source for the drift could be a degradation of the GOMOS or SCIAMACHY instruments (Bramstedt et al., 2009), which is not fully corrected or over-compensated in the level-0 calibration, and the change of the system sensitivities over time.”

34. P16 Line 2: I don’t think I agree with “as proxies for”; I would agree with “to derive”. And to keep this sentence consistent with the next, I’d suggest instead of “excited states” you could have “excited state emissions”.

We changed the sentence to “There are a number of O₂ and O excited state emissions, which can also be used to derive atomic oxygen” in the text according to the referee’s comment.

35. Line 5: There are many more references available. At the very least you need an “e.g.” before the reference.

According to the referee’s comment, we added more references and also “e.g.” in this sentence as “Mostly performed in the 1970s (e.g. Dickinson et al., 1980; Sharp, 1980; Offermann et al., 1981)”

36. Line 6: what is meant by “selective”?

According to the referee’s comment, we modified this sentence to “...and selective in terms of the local time and location” to clarify “selective”.

37. P19 In the conclusions, please also summarize how the new data set compares with those from other instruments.

According to the referee’s comment, we added in the P19 Line 13: “Compared to other datasets derived from various instrument measurements, such as SABER, WINDII, OSIRIS and in situ rocket experiments, the GOMOS data also demonstrates an agreement with these datasets within their combined uncertainties.”

Referee #3

General point:

Probably my major comment is one that I have already given in a similar paper. The authors named the retrieved atomic oxygen as "GOMOS-OH" O, when it is actually additionally based on the external measurements of three key atmospheric quantities: O3, temperature and pressure (density). The authors clearly state this in the introduction and also present an error analysis of these parameters in the retrieved O but, in my opinion, it should also be mentioned in the abstract and in the conclusion. In this way the reader would have a more clear idea of the derived data.

According to the referee’s comment, we added the description about the used external measurements in the abstract (P1 Line 4)

“...on board Envisat, with the SABER measurements for the atmospheric background.”

And also in the conclusion (P19 Line 4)

“...limb measurements, with the atmospheric background profiles of temperature, total density and ozone taken from the SABER measurements.”

Specific points:

1. Title: Is really need the word "resampled".

We deleted “resampled” in the title according to the referee’s comment.

2. Page 1, l. 13. For the sake of clarity I would write " ... by the photolysis of molecular oxygen and of ozone..."

We changed the sentence to “is mainly produced by the photolysis of molecular oxygen and of ozone” in the text to make it clear.

3. Page 5. Interval of wavelength used. The authors justify the limited spectral interval because of problems at longer wavelengths. They state errors of about 12% at these wavelengths. However, from the spectrum shown in Fig. 3, which looks very good at wavelengths of 935-955 nm, and given that 12% is not really large compared to the overall error of about 20%, I wonder if it would not have been useful to include the wider spectral interval. If not, could this be considered

as an additional complexity (potential source of error) of retrieving O from the OH Meinel bands?

The pixel response non-uniformity (PRNU) variation is reported to be around 12% averagely for the entire SPB (SPB1: 755–774 nm & SPB2: 925–955 nm). Our spectrum range of interest is in SPB2, and we found the PRNU changes along the wavelength in SPB2, and a systematic error more than 20% appears in the longer wavelength range. With the SCIAMACHY measurements as reference (Bovensmann et al., 1999), as shown in Fig.3, the radiances at the wavelength range of 935-955 nm are always 25-30% lower in all data points. When the entire spectrum of 925-955 nm is applied in the O retrieval, the derived O is always 25% lower than the SCIAMACHY data. Till now there is no reasonable explanation for this systematic difference between GOMOS and SCIAMACHY at the wavelength range of 935-955 nm (Erkki Kyrölä, personal communication, 2019). Hence, we excluded this wider wavelength in the retrieval.

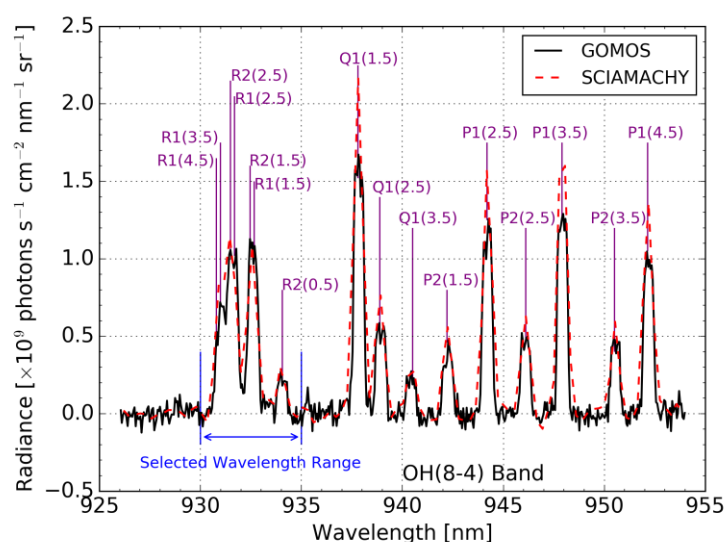


Figure 3. Monthly averaged spectrum from GOMOS (black solid line) for Feb. 2004 at 40°–50° N and at an altitude of 89.5 km. Strong emission lines from OH(8-4) band are annotated with the branch and rotational quantum numbers. The wavelength range from 930 nm to 935 nm is selected and used in the retrieval. The corresponding SCIAMACHY data (red dashed line) is also given here for comparison.

According to the referee's comment, we updated Fig.3 and added a few sentence in P5 Line 8: "As shown in Fig.3, in the spectral range of our interest (SPB2), we found the GOMOS data shows a good agreement with the SCIAMACHY data at the spectral range of 930–935 nm, whereas the GOMOS radiances at the wavelength range of 935-955 nm are always 25-30% lower compared to the SCIAMACHY measurements, which is not understood (E. Kyrölä, personal communication, 2019)."

4. Page 6. Figure caption. Last two lines. Could the authors clarify (give some more details or even an equation) about how the measurement noise of the mean spectra (those used as measurements in the retrieval) were computed? In particular, the mention "integrating", over which quantity? "residual noise standard deviation" residual of what? "spectrum"? I believe they were averaging the spectra in the month/latitude bins, correct? I have no doubt the authors are doing correctly but it would be useful a more detailed description for the readers. Also, please consider moving it to the body text.

The residual noise refers to the noise in the spectrum in between of the emission lines (e.g. 930-930.5 nm & 933-933.5 nm & 934.5 -935 nm). It is called "residual" because in the data processing, the background radiation from above 110 km and the "base" offset are already removed from the spectrum, and the resulted spectrum noise is therefore called "residual"

noise". The procedure to calculate the measurement noise is as follows: calculating the standard deviation of the residual noise outside of the emission lines (σ) → σ is assumed for all wavelengths (the measurement noise is stochastic) → integrating the radiances over all wavelength points (N) of the spectral region → the measurement noise for the integrated radiance is calculated as $\sigma \times \sqrt{N}$ (square root value of the number of points N).

We have updated the error bars for Figure 4, 5 & 12 accordingly.

According to the referee's comment, we moved the description about the measurement noise from the caption of Fig.4 to the body text.

The last sentence in the caption of Fig.4 is modified as: "The error bars indicate the measurement noise for integrated radiance (see text)."

We added in P5 Line 17: "The error bars in the right plot indicate the measurement noise for integrated radiance. The measurement noise is calculated from the standard deviation of the residual noise in the spectral range in between of the emission lines, and assumed to be the same for all wavelengths, as the intensities of remaining weak emission lines from high rotational levels in the spectral region are by several order of magnitude lower and therefore negligible. For the integrated radiance, the measurement noise is increased by a factor of \sqrt{N} , and N refers to the number of integrated wavelength points."

5. Page 7, line 3. "total"? Do they want to say something additional to "the removal of OH(v=8) by O"?

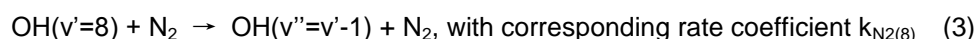
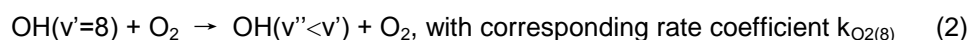
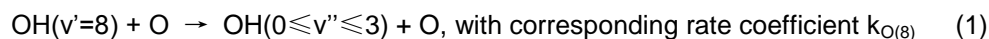
According to the referee's comment, we modified the sentence as "..., the rate coefficients for the production of OH(v=8) by the collision of OH(v=9) with oxygen, and the collisional removal of OH(v=8) by atomic oxygen..."

6. Also, I do not understand why adjusting ONLY this rate for "adjusting the OH(v=8) populations to be consistent with laboratory measurements? Why not, for example, adjusting other rates as, e.g., that with O2? I might be wrong but this seems to me like as ad hoc adjustment with not much justification. Are these uncertainties included in the model error budget?

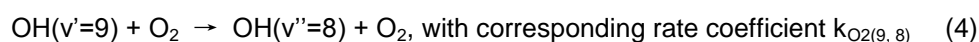
How this rate (OH(v=8) +O) compares to that used/derived by Sharma et al and Panka et al.? In general, could the authors comment on the similarities/differences of the rates affecting OH(8) with those used in other O retrievals from OH? In the conclusion section they mention the possibilities of the discrepancies of this O dataset with other databases possibly caused by differences in the collisional rates. I have no doubt of that but the discussion suggested would be very beneficial to support such conclusion.

(1) Selection of the collisional rate coefficients for OH(v= 8)

A multi-quantum quenching model is applied for the collision of OH radicals with O₂, and the single-quantum quenching is used for the collision with N₂. The total removal rates of OH(v=9) by O₂, k_{O2(9)}, N₂, k_{N2(9)} and O, k_{O(9)} are taken from the laboratory measurements by Kalogerakis et al. (2011, 2016), following Zhu and Kaufmann (2018). The uncertainty of model parameters used in this work are mainly the rate coefficients of the following processes:



and



For the process (1), the determination of the coefficient $k_{O(8)}$ has long been an issue. Some of the reported values for the total removal rate of OH($v=8$) by O from the literature are listed below. These values vary from $4.5 \times 10^{-11} \text{ cm}^3 \text{ s}^{-1}$ to $2.5 \times 10^{-10} \text{ cm}^3 \text{ s}^{-1}$ by nearly one order of magnitude, and currently there are no values being well validated. Therefore, we decided to adjust the rate of this process to bring SCIAMACHY OH(9-6) and OH(8-5) measurements into a consistent picture.

Rate coefficient $k_{O(8)} \times 10^{-10} \text{ cm}^3 \text{ s}^{-1}$	Reference	Source	Note
2.5	Makhlouf et al. (1995)	Empirical estimation	Other relevant parameters are adjusted
2.0	Adler-Golden (1997)	Empirical estimation	Other relevant parameters are adjusted
0.45	Varandas (2004)	Theoretical calculation	
1.0	Copeland et al. (2006)	Laboratory measurement	
0.5	Smith et al. (2010) Mlynczak et al. (2013)	Adjustment to SABER measurement	Other relevant parameters are adjusted
0.65	Xu et al. (2012)	Fitting to SABER measurement	Other relevant parameters are fitted
$0.87 \times (2.3 \pm 1)$	Panka et al. (2017, 2018) Kalogerakis (2019)	Adjustment to laboratory measurement	
1.5	Mlynczak et al. (2018)	Adjustment to SABER measurement	Other relevant parameters are adjusted

For the process (2), the rate coefficients are available from the theoretical calculation or laboratory measurements. Adler-Golden (1997) derived the values of k_{O_2} for every vibrational level as summarized in Table 2, and also provided the laboratory measurements of $k_{O_2(8)}$ in Table 1, as measured by Dyer et al. (1997). These two values of $k_{O_2(8)}$ do not fit with each other. Xu et al. (2012, Table 3 and Figure 7) applied a fitting parameter of 0.723 on the derived values of by Adler-Golden (1997), and brought them into an agreement with the laboratory measurements. This laboratory value is also applied by Mlynczak et al. (2013, Table 1), therefore we took the value from the laboratory measurements in our model.

Rate coefficient $k_{O_2(8)} \times 10^{-12} \text{ cm}^3 \text{ s}^{-1}$	Reference	Source
8 ± 1	Dyer et al. (1997) (Adler-Golden (1997))	Laboratory measurement
11.9	Adler-Golden (1997)	Fitting to airglow measurement
$8.6 (11.9 \times 0.723)$	Xu et al. (2012)	Fitting to SABER measurement
8.0	Mlynczak et al. (2013)	Adler-Golden (1997)

For the process (3), we took the measured value of $k_{N_2(8)}$ by Dyer et al. (1997), which is $k_{N_2(8)} = 7 \pm 4 \times 10^{-13} \text{ cm}^3 \text{ s}^{-1}$. It is applied by Adler-Golden (1997, Table 1), Xu et al. (2012, Table 3), Smith et al. (2010), and Mlynczak et al. (2013, 2018), and Panka et al. (2017, 2018).

For the process (4), Adler-Golden (1997) provided a value of $41.8 \times 10^{-13} \text{ cm}^3 \text{ s}^{-1}$ according to the empirical expression, and Xu et al. (2012) modified it as $30.2 \times 10^{-13} \text{ cm}^3 \text{ s}^{-1}$ with a fitting parameter. Smith et al. (2010) and Mlynczak et al. (2013) also applied a value of $42.0 \times 10^{-13} \text{ cm}^3 \text{ s}^{-1}$ following Adler-Golden (1997). And we firstly applied the value of $42.0 \times 10^{-13} \text{ cm}^3 \text{ s}^{-1}$ in this model.

Rate coefficient $k_{O_2(9,8)} \times 10^{-13} \text{ cm}^3 \text{ s}^{-1}$	Reference	Source
41.8	Adler-Golden (1997)	Fitting to airglow measurement
$30.2 (41.8 \times 0.723)$	Xu et al. (2012)	Fitting to SABER measurement
42.0	Smith et al. (2010) Mlynczak et al. (2013)	Adler-Golden (1997)

A low temperature scale factor is applied for the rate coefficients of OH quenching with O₂ and N₂, which is 1.18 and 1.4 (Lacoursière et al., 2003, Panka et al., 2017), respectively .

(2) Fitting of the selected collisional rate coefficients for OH(v=8)

In this work, specific parameters (e.g. $k_{O(8)}$) are obtained by simultaneously fitting the model to measured limb radiances of OH(9-6) and OH(8-5) bands, as obtained independently from the SCIAMACHY channel 6 measurements. The OH(9-6) band radiance is integrated over the wavelength range of 1378-1404 nm, and the OH(8-5) band is over 1297-1326 nm. The selected parameters are adjusted in such a way that the altitude-resolved ratios of the fitted radiances between the two bands are consistent with the ratios calculated from the measurements. In our study, several cases with different rate coefficients or combinations being adjusted in the fitting are considered.

The comparison of study cases is given in the table below, in which the applied rate coefficients are summarized. The adjusted parameters and their fitted values are marked **bold**, while the coefficients taken from laboratory measurements are underlined and marked *italic*. The fitting results of different cases are illustrated in the figure below, as compared to the SCIAMACHY measurements.

Study case	$k_{O(8)} \times 10^{-10} \text{ cm}^3 \text{ s}^{-1}$	$k_{O_2(8)} \times 10^{-12} \text{ cm}^3 \text{ s}^{-1}$	$k_{N_2(8)} \times 10^{-13} \text{ cm}^3 \text{ s}^{-1}$	$k_{O_2(9, 8)} \times 10^{-13} \text{ cm}^3 \text{ s}^{-1}$
(a)	1.2	<u>8.0</u>	<u>7.0</u>	42.0
(b)	0.65	<u>8.0</u>	<u>7.0</u>	8.9
(c)	0.25	12.0	<u>7.0</u>	42.0
(d)	0.35	<u>8.0</u>	15.0	42.0
(e)	2.0	5.5	<u>7.0</u>	42.0
(f)	2.0	<u>8.0</u>	4.5	42.0

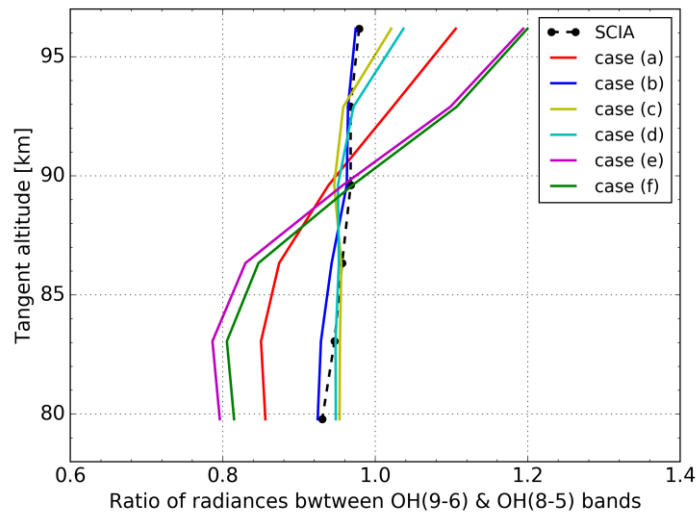


Figure. The ratios of the integrated limb radiances between the OH(9-6) (1378-1404 nm) and OH(8-5) (1297-1326 nm) bands versus altitude. The raw data (black dashed line) is taken from the SCIAMACHY channel 6 measurements. The fitted results (solid line) are obtained by applying the rate coefficients with respect to different cases.

By comparison of the six cases deploying different rate coefficients, it is found that:

1. it is not possible to obtain the optimal fitting by only adjusting one parameters with respect to OH(v=8), i.e. case (a), (e), (f);
2. Combination of $k_{O(8)}$ with one any parameter from $k_{O_2(9, 8)}$, $k_{O_2(8)}$ and $k_{N_2(8)}$, can provide satisfying fitting results, i.e. case (b), (c), (d).

To select the most suitable case of rate coefficients for our work, the following points are considered:

1. It is preferable to apply the fitted value for $k_{O(8)}$, as the values from literature vary by nearly one order of magnitude, and currently there are no values being well validated.
2. The fitted parameters and the laboratory measurements should agree within the combined uncertainties if the laboratory measurements are available. For example, $k_{O_2(8)} = 8 \pm 1 \times 10^{-12} \text{ cm}^3 \text{ s}^{-1}$ and $k_{N_2(8)} = 7 \pm 4 \times 10^{-13} \text{ cm}^3 \text{ s}^{-1}$, as measured by Dyer et al. (1997).
3. Fitting three parameters simultaneously are not considered in our work.

Therefore, we chose and applied case (b) in our work, which is $k_{O(8)} = 0.65 \times 10^{-10} \text{ cm}^3 \text{ s}^{-1}$, and $k_{O_2(9,8)} = 8.9 \times 10^{-13} \text{ cm}^3 \text{ s}^{-1}$.

The obtained rate coefficient for process (4) ($k_{O_2(9,8)}$) is in the order of $10^{-13} \text{ cm}^3 \text{ s}^{-1}$, which is nearly two orders of magnitude smaller than the total removal rate of OH($v=9$) by O_2 ($k_{O_2(9)}$) (Kalogerakis et al., 2011), because most of the collisional loss of OH($v=9$) appears in multi-quantum steps. Since the production rate of OH($v=9$) is assumed to be balanced by its loss, and process (4) leads to an increment of OH($v=8$) population, while this increment is less than 1% compared to the OH nascent production of OH($v=8$). Therefore, we thought the influence of $k_{O_2(9,8)}$ on the population distribution is small that we did not mention this point in the text.

Meanwhile, the process (1), along with process (2) and (3), depopulates the OH($v=8$) radicals. In the mesopause region around 90 km, the density of O, O_2 and N_2 are in the order of 10^{11} , 10^{13} and 10^{13} cm^{-3} . Depending on the orders of magnitude of the rate coefficients for process (1), $k_{O(8)}$, (2), $k_{O_2(8)}$, and (3), $k_{N_2(8)}$, the removal of OH($v=8$) by O may be comparable to the removal by O_2 or N_2 . In this work, $k_{O(8)}$ is in order of $10^{-11} \text{ cm}^3 \text{ s}^{-1}$, $k_{O_2(8)}$ in $10^{-12} \text{ cm}^3 \text{ s}^{-1}$ and $k_{O_2(8)}$ in $10^{-13} \text{ cm}^3 \text{ s}^{-1}$. Hence, the influence of the rate coefficient $k_{O(8)}$ on the population distribution of OH($v=8$) is significant, when the other model parameters are already justified.

To justify these two coefficients, the sensitivity of the retrieval results to the parameter $k_{O(8)}$ and $k_{O_2(9,8)}$ are evaluated in the error analysis, that a 10% perturbation on the parameters lead to a uncertainty of 2%, and 0.5% on the derived O values. Meanwhile, the selection of different fitting coefficients, e.g., the utilization of case c and d will lead to a uncertainty of around 5% above 90 km and 15% at 80 km in the derived abundances.

According to the referee's comment, we modified the description about the rate coefficients in the text to make it accurate: "Additionally, the rate coefficients for the production of OH($v=8$) by the collision of OH($v=9$) with oxygen, and the collisional removal of OH($v=8$) by atomic oxygen are obtained by simultaneously fitting the limb radiances of OH(9-6) and OH(8-5) bands, which are independently taken from the SCIAMACHY measurements. The OH(9-6) band radiance is integrated over the wavelength range of 1378-1404 nm, and the OH(8-5) band is over 1297-1326 nm. These two parameters are adjusted in such a way that the ratio between the fitted radiances of the two bands is consistent with the ratio calculated from the measurements."

We also summarized the above description about the selection of fitting parameters, and added in the Appendix of the text.

A comparison of $k_{O(8)}^p$ ($2.0 \times 10^{-10} \text{ cm}^3 \text{ s}^{-1}$), $k_{O(8)}^m$ ($1.5 \times 10^{-10} \text{ cm}^3 \text{ s}^{-1}$) with $k_{O(8)}^c$ ($0.65 \times 10^{-10} \text{ cm}^3 \text{ s}^{-1}$) is provided in the figure below, as these three values are applied in the OH modeling of this work, and the corresponding ratios of the fitted radiances between the OH(9-6) and (8-5) bands are calculated, respectively. The ratios with both $k_{O(8)}^m$ and $k_{O(8)}^p$ are found to deviate from the measurements. The results indicates there could be a deviation of the population distribution of OH radicals in $v=9$ and $v=8$ by applying different rate coefficients, as compared to the SCIAMACHY measurements. Besides, the retrieval results are affected by the selected value of $k_{O(8)}$. When $k_{O(8)}^p$ and $k_{O(8)}^m$ are applied in our work, the derived O results are found up to 35% and 20% at 95 km larger than before.

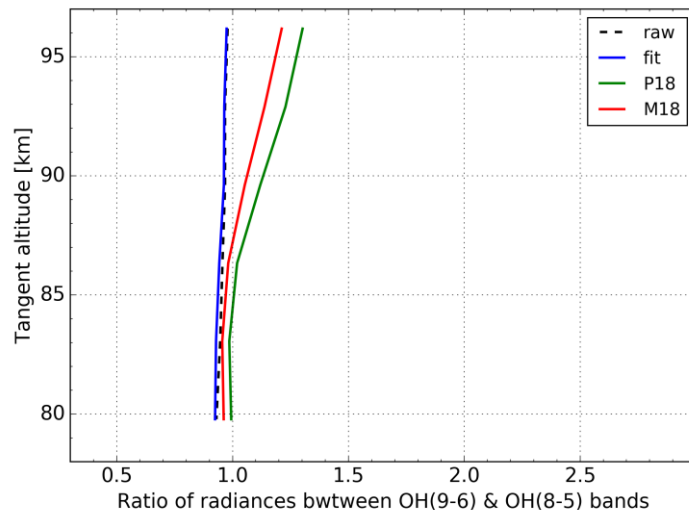


Figure. The ratio of the integrated limb radiances between the OH(9-6) and OH(8-5) bands versus tangent altitude. The raw data (black dashed line) is taken from the SCIAMACHY channel 6 measurements. The OH(9-6) band limb radiance is integrated over the wavelength range of 1378-1404 nm, and the OH(8-5) band is over 1297-1326 nm. The fitted result (blue solid line) is achieved from the fitting, of which the obtained parameters are applied in this work. The M18 (red solid line) applies the value from Mlynzcak et al. (2018) for the rate coefficient of $\text{OH}(v=8) + \text{O}$ in the OH modeling, and P10 (green solid line) applies the one from Panka et al. (2017, 2018).

7. The measurements from Oliva et al. are not laboratory measurements but ground-based nadir atmospheric observations, aren't they?

Yes, they are. According to the referee's comment, we modified the text as in the last answer.

8. Page 7, line 15. "... the a priori information from the real atmospheric state.."? Please clarify: the "real" atmospheric O is used as a priori? This does not make sense. Please be more specific, which O is used as a priori? (I understand from the following text that a priori has a negligible effect but this should be clarified).

The a priori information is not from the real atmospheric state, which is unknown in this case. According to the referee's comment, we modified this sentence as:

"The a priori information about atomic oxygen in this work is taken from MSIS model data, and the zero- and first- order Tikhonov regularization matrices (Tikhonov and Arsenin, 1977) are considered in the cost function."

9. lines 16-17. Which kind (order) of Tikhonov regularization? "Noise is minimized...", which is then the vertical resolution of the retrieved O? This is clearly discussed below, but if you talk about the "noise" at this point you should also mention the vertical resolution.

According to the referee's comment, we modified the sentence in P7 Line 15 as:

"... the zero- and first- order Tikhonov regularization matrices (Tikhonov and Arsenin, 1977) are considered in the cost function. The a priori data about the absolute value of atomic oxygen is taken from MSIS model, which is averaged into the vertical grid of 3 km as the measurements. The first order regularization is obtained from the linear interpolation of the a priori data given on the measurement grid, i.e., no sub measurement-grid information is obtained from that data."

And we added in Line 17 the description about the vertical resolution:

“The vertical resolution of the retrieval results are close to the vertical grid of the measurements.”

10. Page 10, lines 6-7. At which altitude does the discussion in the paragraph above these lines refer to? At the O peak near 95 km? Note that the opposite behaviour is observed (larger values near the equator) in Fig. 8 for, e.g., moths 3, 4, 10 and 11, at an altitude near 90 km. The reader might be confused, as I was.

The discussion in this paragraph refers to the altitude range of 92 - 97 km, where the two-cell structure appears.

According to the referee's comment, we added in P10 Line 2: “Atomic oxygen reveals a two-cell structure near 95 km at mid-latitudes...”

And we added in Line 6: “the atomic oxygen displacement by tides at the mesopause is upward...”

11. Which is the mean local time for each of the plots? Does it change with latitude?

Generally, the mean local time for each plot is around 11 p.m. (10 p.m. to 12 p.m.). The local time is around 11 p.m. in the tropical region, and gradually changes to an earlier/later time with increasing latitude (e.g. 60°N corresponds to the mean local time of around 10 p.m.). The largest variation of local time is found to be in the polar region, which is not considered in this work. In conclusion, the local time of the plot is near midnight. We added in P10 Line 6: “...a local time of almost midnight (the mean local time of the GOMOS measurements is around 11 p.m., 10 p.m. to 12 p.m.), ...”

12. Page 12, line 3. "... solar cycles", caption of Fig. 10, Table 2 and the whole discussion of the solar cycle. The study about the solar cycle(s) has been done assuming that the latest GOMOS measurements analysed, December of 2011, coincides with the maximum of solar cycle 24.

However, this is not fully correct, see

<https://www.swpc.noaa.gov/products/solar-cycle-progression>. This shows that the maximum can be placed somewhere between the 2nd half of 2012 or more likely near the end of 2014. Hence, I suggest that all the discussion, including the two suggested (solarmax and solarmin amplitudes) be revised accordingly. The data presented do not really cover a full solar cycle (see <https://www.swpc.noaa.gov/news/solar-cycle-24-status-and-solar-cycle-25-upcoming-forecast>).

The year 2011 does not coincide with the maximum condition of solar cycle 24, which is more likely to be 2014. Therefore 2011 can not be used as the representative of the solar maximum condition. Since the year 2002 is very close to the maximum condition of solar cycle 23, it could still be used as the proxy. According to the referee's comment, we modified Page 12 Line 2: “...2002 (near solar maximum conditions of solar cycles 23)...”.

Actually, the solar maximum condition for the solar cycle analysis in this work was only based on the year 2002, the maximum condition of the solar cycle 23. Therefore, the year 2011 has no influences on the analyzed results of solar maximum and solar minimum amplitudes.

13. Page 14, line 7. Although mentioned earlier it is very useful to give here the references to the O databases.

According to the referee's comment, we added the references to the O databases in P14 Line 7: “...derived from SCIAMACHY green line emissions (Kaufmann et al., 2014; Zhu et al., 2015) and OH(9–6) band airglow (Zhu and Kaufmann, 2018) ...”

14. Lines 20-21. I would remove the last sentence: "The O ... shown in Fig. 13b". First, because it is not discussed here but later, and also because it additionally contains another O-retrieved profile which is discussed in a different paragraph.

We removed the last sentence in this paragraph according to the referee's comment.

15. I would exchange the order of Figs. 13 and 14.

We exchanged the order of Fig.13 and Fig.14 according to the referee's comment.

16. Fig. 13 is very important as it compares the three O- retrievals. However, for the community, it is more interesting to provide a figure of a GLOBAL comparison of the already published SCIAMACHY OH(9-6) O dataset by Zhu and Kaufmann (2018) with the current dataset. E.g. similar to Fig. 14 but for SCIAMACHY OH(9-6) band instead of SCIAMACHY OH(8-4).

According to the referee's comment, we added in P14 a global comparison of the SCIAMACHY OH(9-6) by Zhu and Kaufmann (2018) with GOMOS OH(8-4) for 2007 as below:

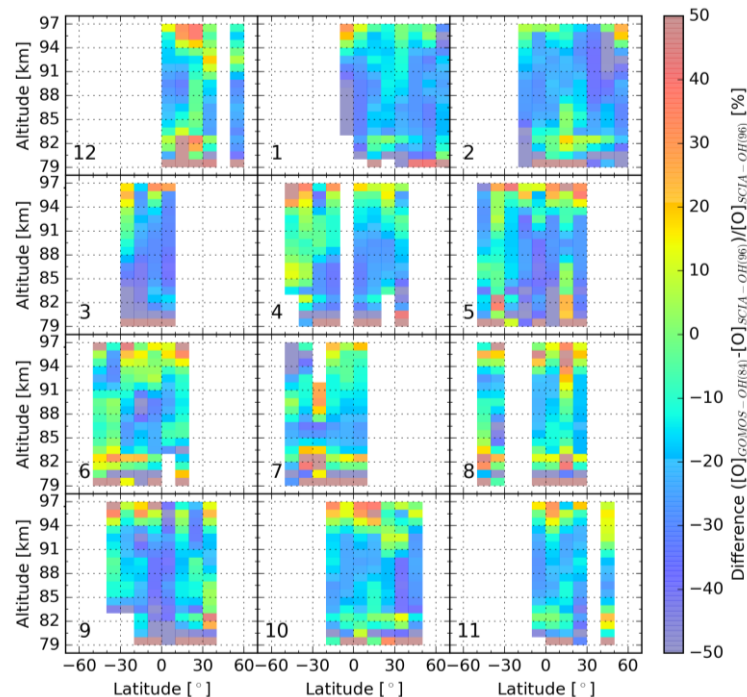


Figure 14. Latitude-altitude distribution of percentage differences between zonal mean atomic oxygen densities derived from GOMOS OH(8-4) and SCIAMACHY OH(9-6) airglow emissions for 2007. The SCIAMACHY OH(9-6) are taken from Zhu and Kaufmann (2018). This figure is plotted in a way similar to Figure 13. Negative numbers indicate that SCIAMACHY OH(9-6) atomic oxygen abundances are larger than the GOMOS OH(8-4) abundances.

And we added in the text the discussion: "Similarly, a latitude-altitude comparison of the GOMOS data with atomic oxygen obtained from SCIAMACHY OH(9-6) emissions (Zhu and Kaufmann, 2018) is given in Figure 16 for 2007. In general, these two dataset agree with each other, but the GOMOS OH(8-4) dataset is found to be around 10-20% lower than the SCIAMACHY OH(9-6) dataset in most latitude bins, especially in the altitude region of 85-95 km. The difference between the two datasets becomes more than 20% at some data points near the equator in March, May and September."

17. Page 14, line 29. Typo SCIAMACHY

We modified the typo according to the referee's comment.

References:

- Adler-Golden, S., Kinetic parameters for OH nightglow modeling consistent with recent laboratory measurements, *Journal of Geophysical Research: Space Physics*, 102, 19 969–19 976, <https://doi.org/10.1029/97JA01622>, 1997.
- Bramstedt, K., S. Noël, H. Bovensmann, J. P. Burrows, C. Lerot, L. G. Tilstra, G. Lichtenberg, A. Dehn, and T. Fehr, SCIAMACHY monitoring factors: Observation and end-to-end correction of instrument performance degradation, in *Proceedings of the 2009 Atmospheric Science Conference[CD-ROM]*, edited by H. Sawaya-Lacoste, ESA Spec. Publ. SP-676, Eur. Space Agency, Frascati, Italy, 2009.
- Copeland, R. A., G. P. Smith, M. M. Mlynczak, and K. S. Kalogerakis, Deactivation of highly vibrationally excited OH by O atoms, *Eos Trans. AGU*, 87(52), Fall Meet. Suppl., Abstract SA21A-0225, 2006.
- Dawkins, E. C. M., Feofilov, A., Rezac, L., Kutepov, A. A., Janches, D., Höffner, J., Chu, X., Lu, X., Mlynczak, M. G., and Russell III, J., Validation of SABER v2.0 operational temperature data with ground-based lidars in the Mesosphere-Lower Thermosphere Region (75-105 km), *Journal of Geophysical Research: Atmospheres*, 123, 9916–9934, <https://doi.org/10.1029/2018JD028742>, 2018.
- Dickinson, P. H. G., Bain, W. C., Thomas, L., Williams, E. R., Jenkins, D. B., and Twiddy, N. D., The determination of the atomic oxygen concentration and associated parameters in the lower ionosphere, *Proceedings of the Royal Society of London. Series A, Mathematical and Physical Sciences*, 369, 379–408, <http://www.jstor.org/stable/2398309>, 1980.
- Dyer, M. J., Knutsen, K., and Copeland, R. A., Energy transfer in the ground state of OH: Measurements of OH($v=8,10,11$) removal, *The Journal of Chemical Physics*, 107, 7809–7815, <https://doi.org/10.1063/1.475094>, 1997.
- Kalogerakis, K. S., A previously unrecognized source of the O₂ atmospheric band emission in Earth's nightglow, *Science Advances*, 5(3), doi:10.1126/sciadv.aau9255, 2019.
- Kalogerakis, K. S., Smith, G. P., and Copeland, R. A., Collisional removal of OH(X², $v=9$) by O, O₂, O₃, N₂, and CO₂, *Journal of Geophysical Research: Atmospheres*, 116, <https://doi.org/10.1029/2011JD015734>, <https://agupubs.onlinelibrary.wiley.com/doi/abs/10.1029/2011JD015734>, 2011.
- Kalogerakis, K. S., D. Matsiev, R. D. Sharma, and P. P. Wintersteiner, Resolving the mesospheric nighttime 4.3 μm emission puzzle: Laboratory demonstration of new mechanism for OH(v) relaxation, *Geophysical Research Letters*, 43(17), 8835–8843, doi: 10.1002/2016GL069645, 2016.
- Lacoursière, J., Dyer, M. J., and Copeland, R. A., Temperature dependence of the collisional energy transfer of OH($v=10$) between 220 and 310 K, *The Journal of Chemical Physics*, 118, 1661–1666, <https://doi.org/10.1063/1.1530581>, <https://doi.org/10.1063/1.1530581>, 2003.
- Makhlouf, U. B., Picard, R. H., and Winick, J. R., Photochemical - dynamical modeling of the measured response of airglow to gravity waves: 1. Basic model for OH airglow, *J. Geophys. Res.*, 100(D6), 11289– 11311, doi:10.1029/94JD03327, 1995.
- Mlynczak, M. G., Hunt, L. A., Mast, J. C., Thomas Marshall, B., Russell, J. M., Smith, A. K., Siskind, D. E., Yee, J.-H., Mertens, C. J., Javier Martin-Torres, F., Earl Thompson, R., Drob, D. P., and Gordley, L. L., Atomic oxygen in the mesosphere and lower thermosphere derived from SABER: Algorithm theoretical basis and measurement uncertainty, *Journal of Geophysical Research: Atmospheres*, 118, 5724–5735, <https://doi.org/10.1002/jgrd.50401>, 2013.

Mlynczak, M. G., L. A. Hunt, J. M. Russell, and B. T. Marshall, Updated SABER night atomic oxygen and implications for SABER ozone and atomic hydrogen, *Geophysical Research Letters*, 45(11), 5735–5741, doi:10.1029/2018GL077377, 2018.

Offermann, D., Friedrich, V., Ross, P., and Zahn, U. V., Neutral gas composition measurements between 80 and 120 km, *Planetary and Space Science*, 29, 747 – 764, [https://doi.org/https://doi.org/10.1016/0032-0633\(81\)90046-5](https://doi.org/https://doi.org/10.1016/0032-0633(81)90046-5), 1981.

Panka, P. A., A. A. Kutepov, K. S. Kalogerakis, D. Janches, J. M. Russell, L. Rezac, A. G. Feofilov, M. G. Mlynczak, and E. Yiğit (2017), Resolving the mesospheric nighttime 4.3 μm emission puzzle: Comparison of the CO_2 (v_3) and OH(v) emission models, *Atmospheric Chemistry and Physics*, 17(16), 9751–9760, doi:10.5194/acp-17-9751-2017.

Panka, P. A., A. A. Kutepov, L. Rezac, K. S. Kalogerakis, A. G. Feofilov, D. Marsh, D. Janches, and E. Yiğit, Atomic oxygen retrieved from the SABER 2.0- and 1.6- μm radiances using new first-principles nighttime OH(v) model, *Geophysical Research Letters*, 45(11), 5798–5803, doi:10.1029/2018GL077677, 2018.

Rodgers, C. D., *Inverse methods for atmospheric sounding: theory and practice*, World Scientific, 2000.

Sander, S., Abbatt, J., Barker, J., Burkholder, J., Friedl, R., Golden, D., Huie, R., Kurylo, M., Moortgat, G., Orkin, V., and Wine, P., *Chemical kinetics and photochemical data for use in atmospheric studies*, Evaluation No. 17, 2011.

Sharma, R. D., Wintersteiner, P. P., and Kalogerakis, K. S., A new mechanism for OH vibrational relaxation leading to enhanced CO_2 emissions in the nocturnal mesosphere, *Geophysical Research Letters*, 42, 4639–4647, <https://doi.org/10.1002/2015GL063724>, 2015.

Sharp, W. E., absolute concentrations of $\text{O}(^3\text{P})$ in the lower thermosphere at night, *Geophysical Research Letters*, 7, 485–488, <https://doi.org/10.1029/GL007i007p00485>, 1980.

Sharp, W. E., The measurement of atomic oxygen in the mesosphere and lower thermosphere, *Planetary and Space Science*, 39, 617–626, 1991.

Smith, A. K., D. R. Marsh, M. G. Mlynczak, and J. C. Mast, Temporal variations of atomic oxygen in the upper mesosphere from SABER, *J. Geophys. Res.*, 115, D18309, doi:10.1029/2009JD013434, 2010.

Noll, S., W. Kausch, S. Kimeswenger, S. Unterguggenberger, and A. M. Jones, OH populations and temperatures from simultaneous spectroscopic observations of 25 bands, *Atmospheric Chemistry and Physics*, 15(7), 3647–3669, doi:10.5194/acp-15-3647-2015, 2015.

Tikhonov, A. and Arsenin, V., *Solutions of ill-posed problems*, Scripta series in mathematics, Winston, <https://books.google.de/books?id=ECrvAAAAMAAJ>, 1977.

Varandas, A. J. C. (2004), Reactive and non-reactive vibrational quenching in $\text{O} + \text{OH}$ collisions, *Chem. Phys. Lett.*, 396, 182–190, doi:10.1016/j.cplett.2004.08.023.

Wold, S., A. Ruhe, H. Wold, and W. J. Dunn, III, The collinearity problem in linear regression. The partial least squares (PLS) approach to generalized inverses, *SIAM Journal on Scientific and Statistical Computing* 1984 5:3, 735-743, 1984.

Xu, J., A. K. Smith, G. Jiang, H. Gao, Y. Wei, M. G. Mlynczak, and J. M. Russell III, Strong longitudinal variations in the OH nightglow, *Geophys. Res. Lett.*, 37, L21801, doi:10.1029/2010GL043972, 2010.

Xu, J., H. Gao, A. K. Smith, and Y. Zhu, Using TIMED/SABER nightglow observations to investigate hydroxyl emission mechanisms in the mesopause region, *J. Geophys. Res.*, 117, D02301, doi:10.1029/2011JD016342, 2012.

Zhu, Y. and Kaufmann, M., Atomic oxygen abundance retrieved from SCIAMACHY hydroxyl nightglow measurements, *Geophysical Research Letters*, 45, 9314–9322, <https://doi.org/10.1029/2018GL079259>, 2018.

Global nighttime atomic oxygen abundances from **resampled** GOMOS hydroxyl airglow measurements in the mesopause region

Qiuyu Chen^{1,2}, Martin Kaufmann^{1,2}, Yajun Zhu^{1,3}, Jilin Liu^{1,2}, Ralf Koppmann², and Martin Riese^{1,2}

¹Institute for Energy and Climate Research, Forschungszentrum Jülich, Jülich, Germany

²Institute for Atmospheric and Environmental Research, University of Wuppertal, Wuppertal, Germany

³State Key Laboratory of Space Weather, National Space Science Center, Chinese Academy of Sciences, Beijing, China

Correspondence: Yajun Zhu (y.zhu@swl.ac.cn)

Abstract. This paper presents a new dataset of nighttime atomic oxygen density [O], derived from OH(8–4) ro-vibrational band emissions, using a non-local thermal equilibrium model, with the aim of offering new insight into the atomic oxygen abundances in the mesopause region. The dataset is ~~based on~~ derived from the level-1 atmospheric background measurements observed by the GOMOS instrument on board Envisat, with the SABER measurements for the atmospheric background. Raw data are reprocessed into monthly zonal mean values in 10° latitude bins with a fixed altitude grid of 3 km. The dataset spans from 70°~~S~~S to 70°~~N~~N in latitude and from 80 km to 100 km in altitude, covering a time period from May 2002 to December 2011 at local times ~~of~~ from 10 p.m. to 12 p.m..

The atomic oxygen density peaks at about 95 km and the highest values are in the range of $3\text{--}8 \times 10^{11}$ atoms cm^{-3} , depending on latitude and season. There is a rapid decrease of [O] below ~~its peak region~~ the peak. The annual oscillation (AO), semiannual oscillation (SAO), and the solar cycle impact are distinguished from the [O] longtime series variations. This new GOMOS [O] dataset conforms to other published datasets and is consistent with the [O] datasets obtained from the SCIAMACHY OH airglow measurements to within about $\pm 20\%$.

1 Introduction

In the middle and upper atmosphere, atomic oxygen (O) is mainly produced by the photolysis of molecular oxygen and ~~ozone~~ photolysis of ozone, and transported downward by diffusion and mixing from the thermosphere to the mesopause. Its lifetime varies from over one week at 100 km to around one day at 80 km due to its increasing chemical loss rate with decreasing altitude (Brasseur and Solomon, 2005). Atomic oxygen is one of the most abundant reactive trace species in the upper mesosphere/lower thermosphere (MLT) region and plays a crucial role in the photochemical equilibrium and energy balance of this region. Most exothermic chemical reactions, which heat the MLT region, are associated with atomic oxygen (Brasseur and Offermann, 1986; Riese et al., 1994; Mlynczak et al., 2013c). The collisions between O and infrared-active greenhouse gases like CO₂ also predominantly lead to radiative cooling in this region (Mlynczak et al., 2013a).

The measurement of atomic oxygen dates back to before the satellite era when the MLT region was explored by means of sounding rocket experiments, hosting resonance fluorescence instruments, or mass spectrometers (~~Dickinson et al., 1974, 1980; Sharp, 1980~~).

(e.g. Dickinson et al., 1974, 1980; Sharp, 1980; Offermann et al., 1981; Sharp, 1991). They are capable of providing direct in situ measurements of atomic oxygen, although it is difficult to obtain a consistent global picture of absolute density values from these measurements, which differ by a factor of more than 40 (Sharp, 1991)(Offermann et al., 1981; Sharp, 1991).

However, these measurements lead to the development of photochemical models of the Earth's day- and nightglow, which enables the use of proxies of the atomic oxygen abundance obtained from satellite observations. Suitable proxies are airglow emissions (e.g. OH*, O₂*, O(¹S)) and thermal emissions (e.g. O₃ at 9.6 μm), in combination with corresponding photochemical models. The hydroxyl (OH) airglow emissions are associated with the spontaneous radiative transitions of excited OH* radicals from higher to lower states. These OH* radicals are mainly produced by the chemical reaction of ozone with atomic hydrogen. Highly excited molecular oxygen O₂* in a metastable state is generated from atomic oxygen recombination and can be de-excited by O or O₂, while the O(¹S) and O₂ A-band emissions are radiated from the products. These airglow emissions rely on the atomic oxygen recombination or ozone destruction, and can be recognized as a kind of chemical afterglow. Therefore, they are frequently used as a proxy to retrieve atomic oxygen.

More recent measurements were conducted by the Sounding of the Atmosphere using Broadband Emission Radiometry (SABER) instrument on the Thermosphere-Ionosphere-Mesosphere Energetics and Dynamics (TIMED) satellite. The instrument detects OH* nightglow radiances at 2.0 and 1.6 μm as well as O₃ thermal emissions at 9.6 μm (Smith et al., 2010; Mlynczak et al., 2013b, 2018; Panka et al., 2018). The Scanning Imaging Absorption Spectrometer for Atmospheric CHatographY (SCIAMACHY) instrument on the European Environmental Satellite (Envisat) measures the O(¹S) green line at 557.7 nm and a broad range of OH* airglow emissions (Kaufmann et al., 2014; Lednyts'kyi et al., 2015; Zhu et al., 2015; Zhu and Kaufmann, 2018). The Optical Spectrograph and Infrared Imager System (OSIRIS) instrument on the Odin satellite probes the O₂ A-band at 762 nm and OH* airglow at 725–745 nm and 770–815 nm (Sheese et al., 2011, 2014). During the period 1991–1995, the Wind Imaging Interferometer (WINDII) instrument on board the Upper Atmosphere Research Satellite (UARS) also observed the O(¹S) green line and OH(8–3) band emissions at 734 nm (Russell and Lowe, 2003; Russell et al., 2005). Other instruments include the High Resolution Doppler Imager (HRDI) on board UARS, which also observes O₂ A-band emissions (Hays et al., 1993); the Imager of Sprites and Upper Atmospheric Lightning (ISUAL) instrument on board the FORMOSAT-2 satellite, which detects the O(¹S) green line emissions (Gao et al., 2012); and the Solar Mesosphere Explorer (SME) spacecraft, which measures the OH(7–5) band emission at 1.87 μm (Thomas, 1990).

While various datasets are consistent in terms of the overall profile shape of derived [O] densities, some discrepancies still exist (Mlynczak et al., 2013c, a, b; Kaufmann et al., 2014; Mlynczak et al., 2018; Zhu and Kaufmann, 2018; Panka et al., 2018). The radiometric calibration of the instruments or differences in airglow model parameters are potential reasons. Therefore, no common consensus has generally been reached with regard to these aspects. Some new findings on airglow relaxation modeling and reaction kinetic parameters were recently published. A new pathway, in which highly vibrationally excited OH radicals ($v \geq 5$) are deactivated by atomic oxygen to a lower state ($0 \leq v' \leq v-5$) is proposed and discussed (Sharma et al., 2015; Kalogerakis et al., 2016; Panka et al., 2017, 2018; Fytterer et al., 2019; Kalogerakis, 2019). These results complicate the topic further.

To contribute another piece of information to the currently ongoing discussions, a new dataset derived from the OH nightglow observed by the GOMOS (Global Ozone Monitoring by Occultation of Stars) instrument on the ~~Envisat~~ ESA's (European Space Agency) environmental satellite (Envisat) during the years 2002 to 2012 is presented and discussed here. This dataset is particularly valuable in that it was obtained at the same time as the already published SABER and SCIAMACHY data, but
5 from a different instrument with its own radiometric calibration. Emissions from OH($v=8-4$) are used to obtain atomic oxygen abundances, which is a similar proxy as provided by the SABER and SCIAMACHY OH measurements.

This paper is structured as follows: the second section provides a brief introduction to the instrument and data processing procedure, followed by a section describing the airglow modeling. The derived results are shown in the fourth section, including error analysis as well as latitudinal and temporal analysis. The next section investigates the validation of the dataset in a broad
10 context, including comparisons with the SCIAMACHY dataset and other data sources, while the final section concludes the topic with an outlook on future expectations.

2 Measurements and Data Preparation

2.1 GOMOS on Envisat

The GOMOS (~~Global Ozone Monitoring by Occultation of Stars~~) spectrometer is one of nine instruments on board ~~the~~
15 ~~ESA's (European Space Agency) environmental satellite (Envisat)~~ Envisat. It is designed to monitor ozone profiles and other ~~entities mostly trace species~~ using stellar occultation and atmospheric transmission measurements in limb-viewing mode (ESA, 2010). Envisat follows a ~~Sun-synchronous orbit with a descending node~~ sun-synchronous orbit with an equator crossing time (descending node) of 10 p.m. (Gottwald et al., 2011). The operation period of GOMOS dates from April 2002 to April 2012. However, there was an instrument malfunction in summer 2005, resulting in a data gap of nearly three months. The GOMOS
20 instrument delivers one vertical profile of measurements for each occultation, and the altitude coverage spans from 5 km to 150 km, with a vertical sampling rate of better than 2 km (Kyrölä et al., 2012). It has four spectral channels in the ultra-violet to near-infrared spectral range. The spectrometer B2 (SPB2), which provides the data used in this work, covers 925–955 nm with a spectral resolution of 0.13 nm at full width half maximum (FWHM) and a sampling step of 0.056 nm (Massimo Cardaci and Lannone, 2012). The GOMOS detector has three parallel bands. The central band probes the star spectra and the upper/lower
25 bands record the atmospheric background radiation as calibration information, as indicated in Figure 1. The altitudes of tangent points observed by three bands differ roughly by 1.7 km. OH and O₂ A-band are regularly detected in the upper/lower bands, together with auroral ~~lights emissions~~ and the stray light scattered by particles or molecules in the atmosphere. This dataset, which is used in our analysis, is archived in the level-1b limb dataset but not directly utilized in the operational level-2 data retrieval routines. First analyses of the extracted OH and O₂ A-band nightglow measurements from these background datasets
30 were reported by Bellisario et al. (2014).

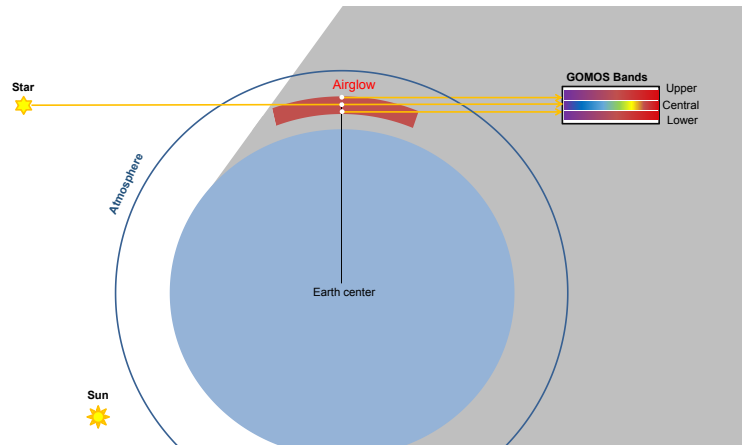


Figure 1. Schematic view of the GOMOS stellar occultation observations. The star transmission spectra are recorded in the central band of the instrument detector, while the atmospheric background radiation is imprinted in the upper/lower bands. The O_2 A-band and OH airglow emissions are detected in the limb observations. For each star spectrum, one upper and one lower ~~spectra~~ spectrum are recorded simultaneously.

2.2 Data Selection and Resampling

The GOMOS data were processed with the processor version 6.01–2012. The resulting level-1b limb products have already been geolocated and calibrated (Massimo Cardaci and Lannone, 2012). The signal-to-noise ratio (SNR) of single spectra is on the order of one, and the averaging of data is required for further processing of the data.

- 5 The raw data from level-1b limb products are first filtered with the corresponding auxiliary “quality flag” and “product confidence data”(PCD), which indicate the presence of bad pixels, saturation, cosmic rays, modulation, dark current, flat-field or vignetting correction, with only data in the normal status being kept. This is then followed by a geolocation-related selection, in which the data with ray-tracing errors are eliminated, and their star IDs and geolocation errors are restricted to within an acceptable range, as recommended by Dehn (2012). The stray light entering the field of view (FOV) of the instrument affects the illumination of the spectrometer and enhances the background noise. The stray light is characterized by the illumination flags and solar zenith angle (SZA) of satellite and tangent points, which are geometrically computed. The illumination conditions of GOMOS measurements are categorized into five flags (Kyrölä et al., 2010; van Gijssel et al., 2010), and the “bright limb” flag thereof is excluded in this work. $SZA > 108^\circ$ is also applied as selection criteria. Near-infrared aurora at wavelengths of around 939 nm and 947 nm, originating from the atomic nitrogen (N I) emissions and N_2^+ Meinel (2–1) band (Baker et al.,
- 10 1977) are in the spectral range of SPB2. Observations in polar regions are therefore not considered in our analysis.

Due to the nature of the stellar occultation observations, the tangent points of single vertical profiles diverge significantly and are not stationary in latitude-longitude locations. In the level-2 product, they are characterized by the obliquity (Kyrölä et al., 2010), which is not available in the level-1b data. Therefore, in this work, the latitude ~~deviation~~ spread of tangent points

is used instead and profiles with $> 4^\circ$ deviation in tangent point latitudes are disregarded to ensure that every selected profile spans a geographical area of within $\pm 5^\circ$ [latitude](#).

The archived ~~Level-1b~~ [level-1b](#) data are signals recorded by the detector, which must be dynamically decoded to electrons and then converted to a physical unit of flux with wavelength-specific radiometric calibration factors. [The star is a point source, and part of the stellar light is spread to the lower and upper band, which is supposed to be totally imaged in the central band in an ideal case.](#) Considering the contamination of star leakage ~~from the central band~~ and residual stray light, which are assumed to be constant with altitude, the averaged spectra from above 110 km are subtracted from each profile as background radiation. No airglow emissions are found above the region of 110 km in the GOMOS measurements. The subtraction is then followed by the individual “base” removal at each altitude layer, in which this “base” offset is the mean of residual noise of the emission lines. The processed data are resampled into monthly and zonally averaged 10° latitude bins with a fixed altitude grid of 3 km to enhance the spectra SNR and improve retrieval quality. The number of profiles selected for one sample bin (shown in Figure 2) is around 100 to ~~300 with a large geospatial variation.~~ [300](#). In order to eliminate the effect of random and systematic noise as well as outliers while retaining as many profiles as possible, the largest and smallest 1% are disregarded from the measurements at each sample bin [for the resampling](#).

Barrot et al. (2003) reported high pixel response non-uniformity (PRNU) variation of around 12% in spectrometer B (SPB) ~~during flight. After careful investigation, this was found to arise especially in the~~. [As shown in Figure 3, in the spectral range of our interest \(SPB2\), we found the GOMOS data shows a good agreement with the SCIAMACHY data at the spectral range of 930–935 nm, whereas the GOMOS radiances at the wavelength range of ~~937 to 950 nm~~ 935–955 nm are always 25–30% lower compared to the SCIAMACHY measurements, which is not understood \(E. Kyrölä, personal communication, 2019\).](#) Therefore, of the entire ~~OH(8–4) band~~ [spectral range](#), only the wavelength region of 930–935 nm is utilized in the retrieval to derive the atomic oxygen abundances. It includes ~~three emission lines in the R₁ branch~~ [a number of emission lines from OH\(\$v=8-4\$ \) band, which originates from the radiative transitions of OH\(\$v'=8\$ \) \$\rightarrow\$ \$v''=4\$ \).](#) The dominant emission lines are mainly in the R branch with a rotational [state](#) quantum number of $J' - K'' = 2.5, 3.5, \text{ and } 4.5$ (illustrated in Figure 3). [1, 2, and 3.](#)

The [quality of the](#) reprocessed spectra are ~~quantified-evaluated~~ by calculating the standard deviation (STD) of averaged spectra for each sample bin, supplemented by ~~SNR~~ [the SNR analysis](#). The calculations show that the mean STD for a typical sample bin in autumn at mid-latitudes is around $2-4 \times 10^9$ photons $\text{s}^{-1} \text{cm}^{-2} \text{nm}^{-1} \text{sr}^{-1}$, and that SNR increases to ~~higher-more~~ than 10 at peak altitudes and [to](#) around 3–5 at lower altitudes. A typical profile of processed hydroxyl spectra and integrated radiance are illustrated in Figure 4. Three ~~radiance peaks are clearly recognizable~~ [lines are clearly visible](#) in the spectra (left), while the emission peak layer appears at [the tangent altitude of](#) around 85 km, according to the right-hand side plot. [The error bars in the right plot indicate the measurement noise for integrated radiance. The measurement noise is calculated from the standard deviation of the residual noise in the spectral range in between of the emission lines, and assumed to be the same for all wavelengths, as the intensities of remaining weak emission lines from high rotational levels in the spectral region are by several order of magnitude lower and therefore negligible. For the integrated radiance, the measurement noise is increased by a factor of \$\sqrt{N}\$, and N refers to the number of integrated wavelength points.](#)

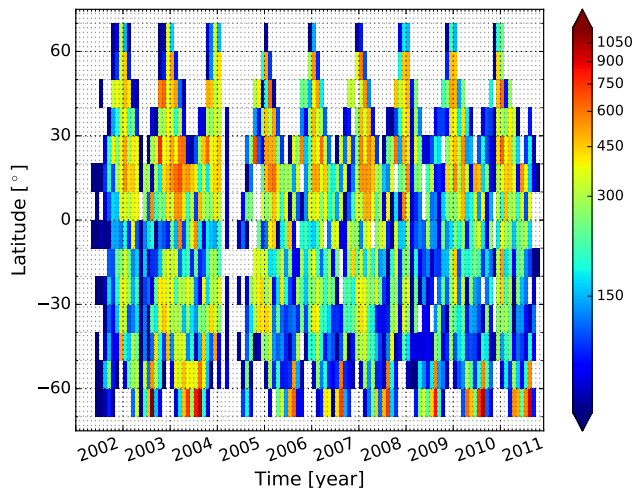


Figure 2. Latitudinal distribution of resampled GOMOS data available from 2002 to 2012. Colour coding indicates the number of selected profiles for each monthly and zonally averaged 10° latitude bin.

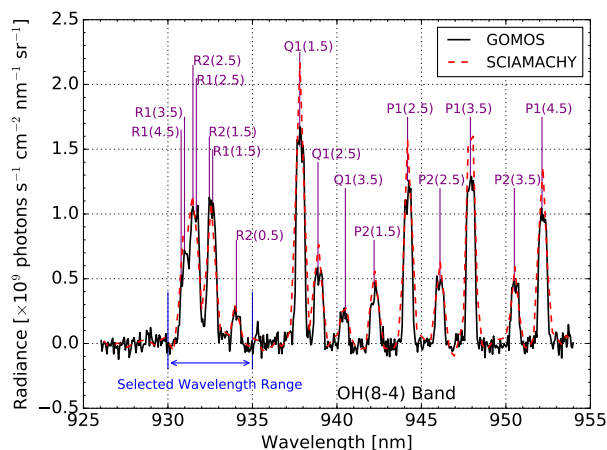


Figure 3. Monthly averaged spectrum [from GOMOS \(black solid line\)](#) for Feb. 2004 ~~is given as an example~~ at 40° – 50° N and at an [a tangent](#) altitude of 89.5 km. [Strong emission lines from OH\(8–4\) band are annotated with the branch and rotational quantum numbers.](#) The wavelength range from 930 nm to 935 nm is selected and used in the retrieval. [The corresponding SCIAMACHY data \(red dashed line\) is also given here for comparison.](#)

3 OH Airglow Modeling and Retrieval Methods

The method to derive atomic oxygen abundance relies on the chemical equilibrium between ozone production and loss during nighttime. It is also applied for the retrieval of atomic oxygen abundances from SABER (Mlynczak et al., 2018) and SCIAMACHY (Zhu and Kaufmann, 2018) OH measurements. Ozone is produced in the three-body recombination reaction

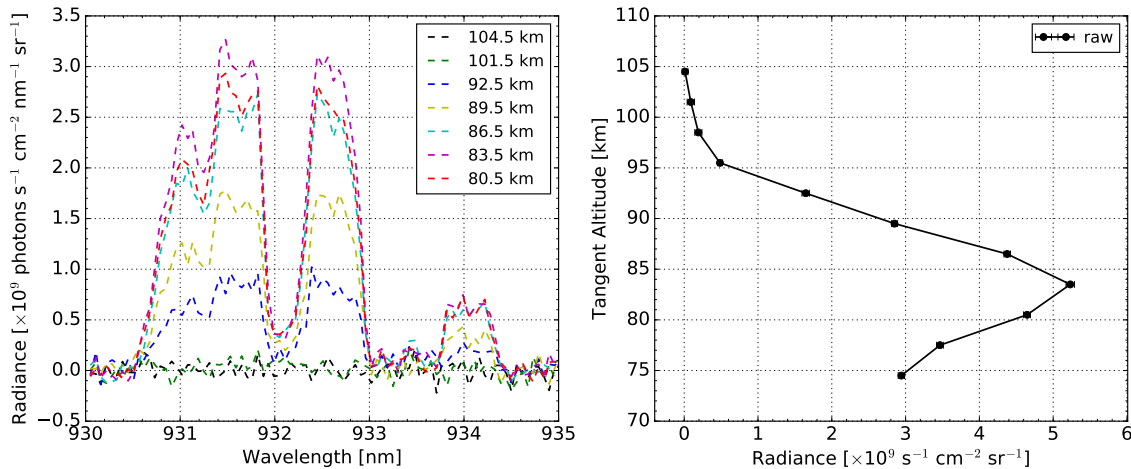


Figure 4. (left) GOMOS monthly zonal mean spectra of OH(8–4) emissions at tangent altitudes as given in the figure legend for Oct. 2003 at 0° – 10° S and at a local time of 10–12 p.m.. (right) The spectrally integrated radiance over 930–935 nm versus tangent altitude for the same conditions. The error bars indicate measurement noise, which is computed by integrating the residual measurement noise standard deviation across the spectrum for integrated radiance (see text).

of atomic and molecular oxygen. Ozone is destroyed in reactions with atomic hydrogen and oxygen. Most As summarized in Table 1, most of the model parameters are adopted from Zhu and Kaufmann (2018). Additionally, the rate coefficients for the production of OH($v=8$) by the collision of OH($v=9$) with oxygen, and the total removal rate coefficient collisional removal of OH($v=8$) by atomic oxygen is are obtained by simultaneously fitting the limb radiances of OH(9–6) and OH(8–5) bands, which are independently taken from the SCIAMACHY measurements. These two parameters are adjusted in such a way that the OH vibrational population density of $v=8$ ratio between the fitted radiances of the two bands is consistent with laboratory measurements (Cosby and Slanger, 2007; Oliva et al., 2015), as summarized in Table 1 the ratio calculated from the measurements. Details about the fitting of the parameters are provided in the Appendix A.

Atmospheric background profiles of temperature, total density, and ozone mixing ratio are taken from SABER measurements (v2.0–2016). The same latitude bins ($\pm 5^{\circ}$) and local times (± 1 hour) were selected for SABER data as GOMOS data. Since SABER cannot measure O_2 and N_2 mixing ratios, these quantities are taken from the mass spectrometer incoherent scatter (MSIS) simulation model data (Picone et al., 2002).

The inverse model applies a constrained global-fit approach following the formalism of Rodgers (2000). The target parameters are the vertical profiles of atomic oxygen abundances, complemented by variables describing the spectral resolution, a wavelength shift, which both are altitude-independent. The content of information in the spectra is sufficient to retrieve these additional parameters. They are capable of reproducing the spectrum characteristics, which cannot be fully captured only by regulating oxygen densities in the model, thus resulting in a better agreement between measured and simulated spectra. Besides, the a-priori information from the real atmospheric state is considered as the regularization term for the retrieval. The Tikhonov

Table 1. OH airglow modeling parameters used in this study, where k_1 to k_3 represent the chemical reaction rate coefficient; f_9 and f_8 refer to the sum of Einstein coefficients of spontaneous transitions from vibrational level $v=9$ or 8 ; and k_{N_2} , k_{O_2} , and k_O represent the quenching coefficients of OH^* radicals by N_2 , O_2 , and O .

Parameter	Process	Rate Constant	Reference
k_1	$O + O_2 + M$	$6.0 \times 10^{-34} (300/T)^{2.4} cm^6 s^{-1}$	Sander et al. (2011)
k_2	$H + O_3$	$1.4 \times 10^{-10} exp(-470/T) cm^3 s^{-1}$	Sander et al. (2011)
k_3	$O + O_3$	$8.0 \times 10^{-12} exp(-2060/T) cm^3 s^{-1}$	Sander et al. (2011)
f_9 & f_8	OH^* nascent branching factor	0.47 & 0.34	Adler-Golden (1997)
$k_{N_2(8)}$	$OH(8) + N_2$	$^a 1.4 \times (7 \pm 4) \times 10^{-13} cm^3 s^{-1}$	Adler-Golden (1997) (Table 1, measured by Dyer et al. (1997))
$k_{O_2(8)}$	$OH(8) + O_2$	$^a 1.18 \times (8 \pm 1) \times 10^{-12} cm^3 s^{-1}$	Adler-Golden (1997) (Table 1, measured by Dyer et al. (1997))
$k_{O(8)}$	$OH(8) + O$	$6.5 \times 10^{-11} cm^3 s^{-1}$	this work
$k_{O_2(9,8)}$	$OH(9) + O_2 \rightarrow OH(8) + O_2$	$^a 1.18 \times 8.9 \times 10^{-13} cm^3 s^{-1}$	this work
$k_{N_2(9)}$	$OH(9) + N_2$	$^a 1.4 \times (7 \pm 2) \times 10^{-13} cm^3 s^{-1}$	Kalogerakis et al. (2011)
$k_{O_2(9)}$	$OH(9) + O_2$	$^a 1.18 \times (2.2 \pm 0.6) \times 10^{-11} cm^3 s^{-1}$	Kalogerakis et al. (2011)
$k_{O(9)}$	$OH(9) + O$	$(2.3 \pm 1) \times 10^{-10} cm^3 s^{-1}$	Kalogerakis et al. (2016)

^a A low temperature scale factor, as the mesopause temperature is normally much lower than the laboratory conditions (Lacoursi re et al., 2003; Panka et al., 2017).

~~regularization matrix (Tikhonov and Arsenin, 1977) is therefore included and accordingly adjusted so that the influence of measurement noise is minimized and Gauss-Newton iterative method in the n-form (Rodgers, 2000, p. 85) is chosen to minimize the cost function of this inverse problem. Besides, a priori information about the atmospheric state is included in the retrieval for regularization to mitigate the influence of measurement errors. The a priori information about atomic oxygen in this work is taken from MSIS model data, and the results are constrained in a physically reasonable domain zero- and first- order Tikhonov regularization matrices (Tikhonov and Arsenin, 1977) are considered in the cost function. The a priori data about the absolute value of atomic oxygen is taken from MSIS model, which is averaged into the vertical grid of 3 km as the measurements. The first order regularization is obtained from the linear interpolation of the a priori data given on the measurement grid, i.e., no sub measurement-grid information is obtained from that data. The regularization strength depends on altitude and its main purpose is to assure meaningful values at the upper and lower boundaries of the altitude regime considered. In between, the regularization has virtually no effect on the retrieved quantities, as can be seen from the retrieval diagnostics. The vertical resolution of the retrieval results are close to the vertical grid of the measurements. The target parameters of the retrieval are the vertical profiles of atomic oxygen abundance, spectral resolution, and a wavelength shift. The latter are both altitude-independent and give a better agreement between measured and simulated spectra. The content of information in the spectra is sufficient to retrieve these additional parameters.~~

4 Results

4.1 Atomic Oxygen Abundances

Applying the global fitting method to GOMOS level-1b limb products, a globally distributed longtime time series [O] dataset is derived, along with other quantities. The fitted spectra are compared with the measurements as shown in Figure 5-5 (left) is a typical profile of the fitted spectra compared with the measurements. In general, they simulations and measurements are in good agreement. The spectrally integrated radiances in Figure 5-5 (right) also show consistency. The typical value of retrieved spectral resolution is around 0.48 nm, and no wavelength shift is found. The derived oxygen densities are within an altitude range of 80 km to 100 km, covering the period from May 2002 to December 2011 and spanning local times from 10:00 p.m. to 12:00 p.m.. A typical atomic oxygen profile is shown in Figure 6 with a maximum concentration of about 3.5×10^{11} atoms cm^{-3} at 95 km. Above the maximum, there is a downward flux of atomic oxygen by diffusive transport (Swenson et al., 2018). Turbulences associated with gravity wave breaking, along with damped waves or tides, are the dynamic processes that contribute to this diffusive transport (Smith et al., 1987; Li et al., 2005). Below the maximum, there is a rapid decrease in atomic oxygen density, which is mainly due to the vertical transport and chemical losses. At an altitude of around 85 km, atomic oxygen density already declines by one order of magnitude to 10^{10} atoms cm^{-3} . The typical value of simultaneously retrieved spectral resolution is around 0.48 nm, and no wavelength shift is found.

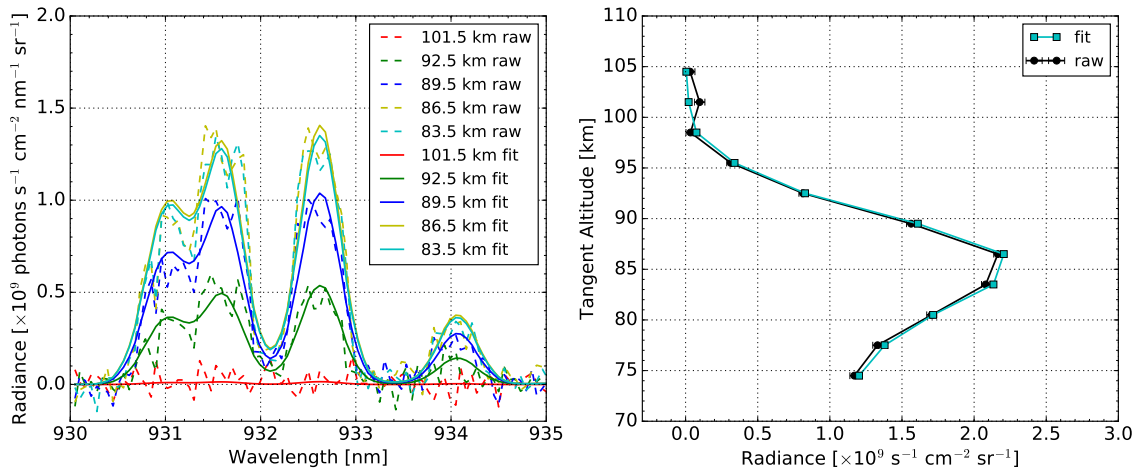


Figure 5. (left) Simulated spectra (fit, solid line) and measurements (raw, dashed line) of GOMOS monthly zonal mean measurements of OH(8-4) airglow emissions at tangent altitudes, as given in the figure legend for Feb-Aug. 2006-2003 at 1030° - 20° N- 40° S and a local time of 10-12 p.m.. (right) The spectrally integrated radiance over 930-935 nm versus tangent altitude for the same conditions.

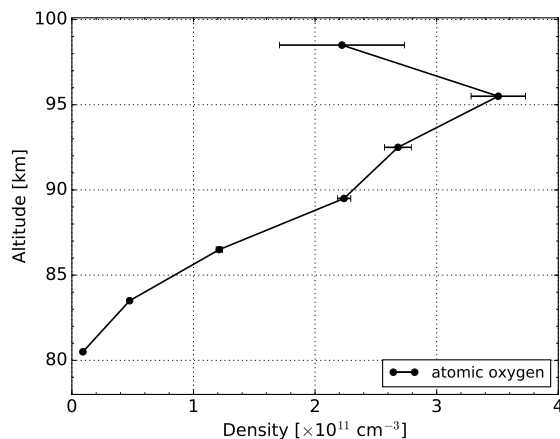


Figure 6. Atomic oxygen abundances, derived from GOMOS monthly zonal mean measurements of OH(8–4) airglow emissions for Feb. 2006 at 10° – 20° – N° – N . The error bar represents the statistical uncertainty coming from the measurement noise. It increases towards higher altitudes, as a consequence of the corresponding SNR being ~~lower~~lesser.

4.2 Error Analysis

The ~~accuracy~~total uncertainty of the derived atomic oxygen densities not only depends on the measurement noise, but also on the smoothing error as well as ~~the~~on uncertainties in forward model parameters and the background atmosphere input. The largest source of uncertainties is found in the forward model parameters. The influence of these uncertainties on the results are assessed through error propagation, by the perturbation of forward model parameters. The chemical reaction rate coefficient k_1 has an uncertainty of around 20%, contributing around 15% uncertainty below 90 km and around 20% at 95 km in derived abundances. k_3 introduces an increasing uncertainty of up to 6% at 95 km. The nascent branching factor (e.g. f_8, f_9) explains the distribution ratio of excited hydroxyl radicals OH* of different vibrational levels. f_8 has a linear influence on the uncertainty of the results; a perturbation of 10% on its values results in a similar retrieval uncertainty. The errors of Einstein coefficients correspond to an uncertainty of around 7% in the results. The ~~quenching coefficient~~ $k_{O_2(8)}$ uncertainty in the quenching coefficient $k_{N_2(8)}$ of OH* radicals with oxygen molecules-nitrogen molecules introduces a uncertainty of 14% at 80 km, which decreases to 5% at 95 km, and the uncertainty in the rate coefficient for quenching by molecular oxygen $k_{O_2(8)}$ corresponds to an uncertainty of 5% ~~and the~~ at 85 km and 2% at 95 km. The influences of other model parameters are ~~in~~on the order of 1–2% or less. SABER temperature uncertainties are the predominant factor influencing the retrieval results in the background atmosphere. The uncertainties are around 5.5 K at 80 km and increase to 13 K at 90 km (Dawkins et al., 2018). This Through error propagation calculation, this could lead to an uncertainty of 5% below 90 km and up to 20% above 95 km, taking into account the compensation effects of total density changes following the hydrostatic equilibrium (Zhu and Kaufmann, 2018).

At the altitude of 80–100 km, the effects of the smoothing error and measurement noise on the uncertainty are on the order of around 0.5% and 5%, respectively. It is due to a properly chosen regularization in the retrieval procedure that the a priori information is negligible in the retrieval results. As part of a more in-depth look into the retrieval results, the average-averaging kernel and vertical resolution are investigated, as shown in Figure 7. The total-average-kernels-summed-up averaging kernels for each row in the altitude region of interest (80–100 km) are equal to one, indicating that the measurements instead of the a priori information contribute to nearly all of the retrieval result. The peaks of average-averaging kernels are found at the tangent altitudes and the corresponding vertical resolution for each altitude is around 3 km. It is consistent with the input altitude grid of 3 km, referring to the retrieval information mainly originates from the atmospheric state of the tangent point and is strictly constrained in the proximately vertical sampling grid of 3 km, which is close to the vertical spacing of the limb measurements.

10 Since the sum of the averaging kernels is also near one, the a priori influence is generally low.

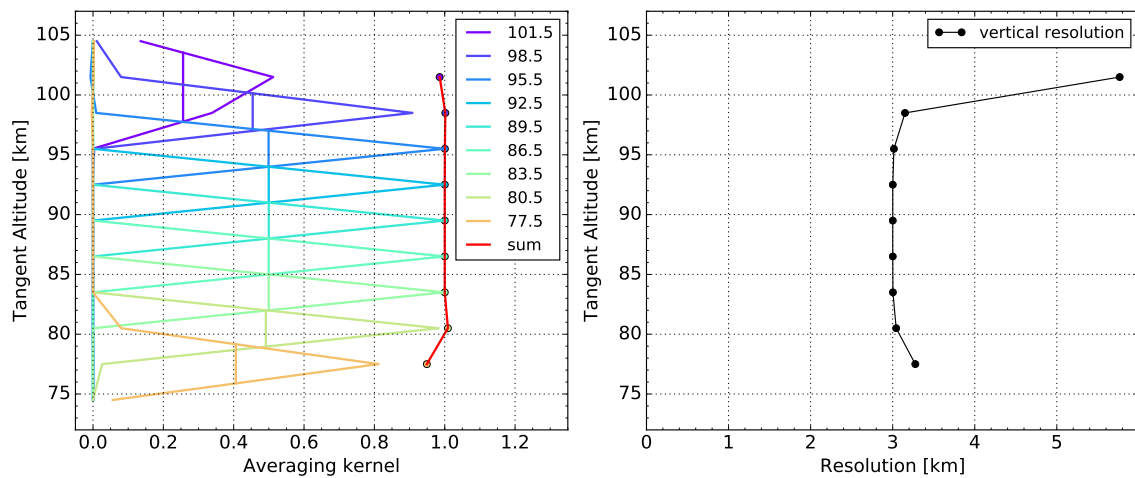


Figure 7. (left) The average-averaging kernel and (right) the vertical resolution of the retrieval for Feb. 2006 at 10° – 20° N and a local time of 10–12 p.m.. The retrieval-altitude-grid-refers-to-the vertical resolution of the derived quantities and is equal to obtained from the FWHM distribution of average kernels each row in the averaging kernel by calculating the corresponding altitude layers FWHM.

4.3 Spatial and Temporal Analysis

Atomic oxygen reveals a two-cell structure near 95 km at mid-latitudes, which is most pronounced during the equinox seasons (Figure 8). The smallest values appear over the equatorial region and the largest values are at mid-latitudes. As already mentioned and discussed by Smith et al. (2010), this and Xu et al. (2010), the latitudinal distribution structure of atomic oxygen is influenced by local-time-dependent migrating diurnal tides, which have a maximum wind amplitude over the equator and two weaker maxima of opposite signs at mid-latitude tides. The vertical transport of air caused by tides leads to a vertical displacement of atomic oxygen. At a local time of almost midnight (the mean local time of the GOMOS measurements is

15

around 11 p.m., 10 p.m. to 12 p.m.), the atomic oxygen displacement by tides at the mesopause is upward at the equator (resulting in an [O] decrease) and downward in subtropical latitudes (resulting in an [O] enrichment).

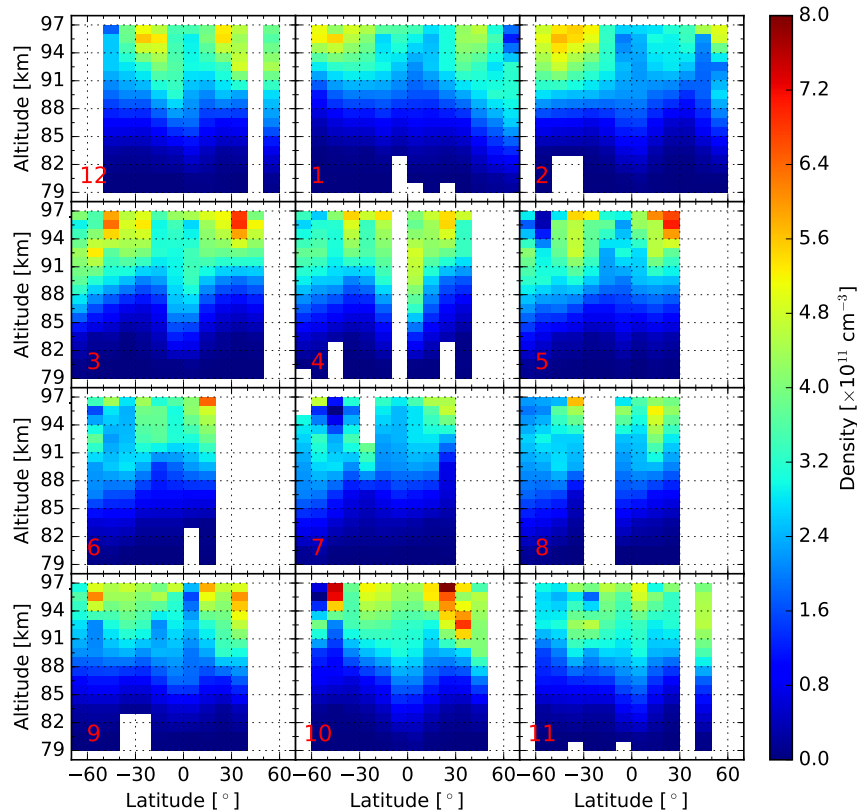


Figure 8. Latitude-altitude distribution of the zonal mean atomic oxygen density for 2007. Each row represents approximately a season. The data are linearly interpolated into a 1 km altitude grid for better illustration. The numbers in the subplots indicate the month of the year.

In Figure 9, a vertical distribution comparison of derived densities from 2002 to 2011 over the mid-latitude and equatorial regions is shown. Both the annual oscillation (AO) and semiannual oscillation (SAO) can be seen from the temporal evolution of mid and lower latitudes. The SAO reaches its maximum at equinox seasons, which is related to the semiannual variation of the atmospheric tide amplitudes (Smith et al., 2010).

A multiple linear regression analysis is applied to quantitatively analyze the longtime variations of the GOMOS [O] dataset. The monthly mean column density integrated from 80–97 km for 20°–30°N is analyzed by the harmonic fitting, which includes components such as the solar cycle effect, SAO, AO and QBO (quasi biennial oscillation), and offset baseline.

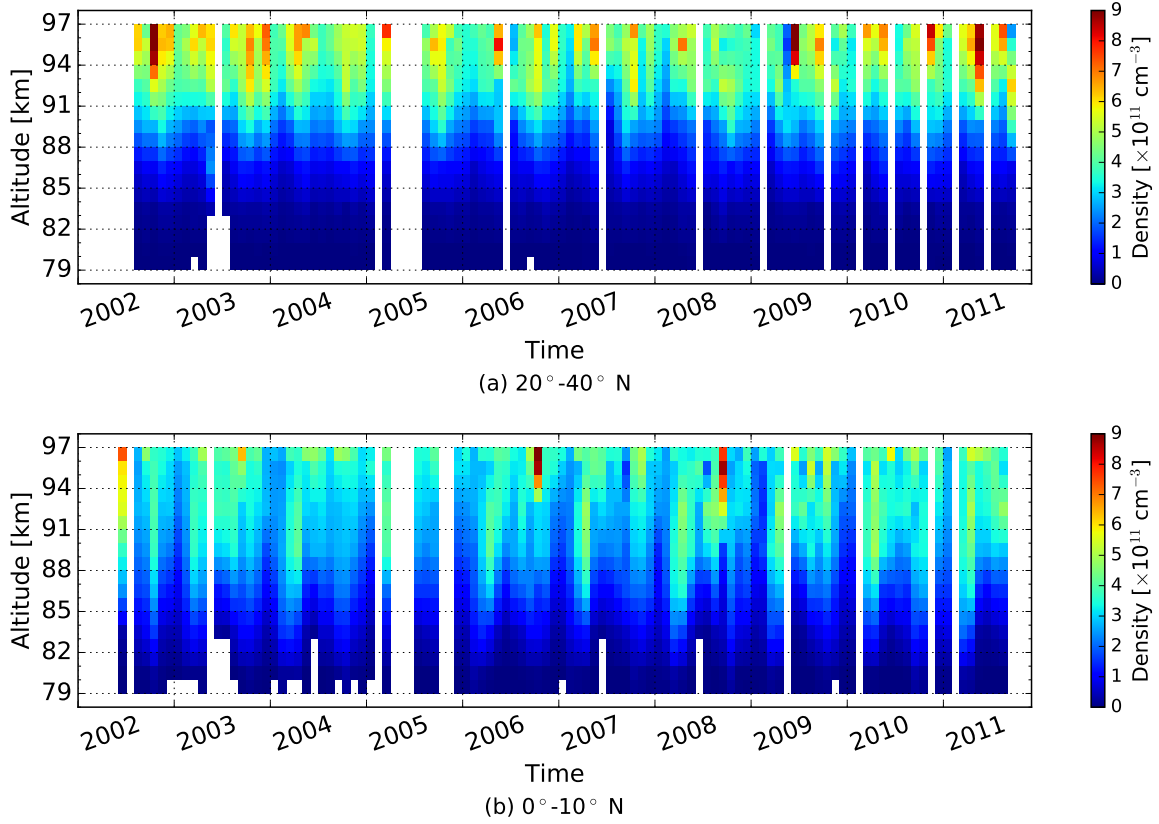


Figure 9. Temporal evolution of the vertical distribution of monthly zonal mean atomic oxygen densities for 20° - 40° - N - N (a) and 0° - 10° - N - N (b). The data are linearly interpolated into a 1 km altitude grid.

$$[O]_{Column} = \text{Offset} + A_{solar} \cdot I_{solar} \cdot (t + \text{shift}) + A_{SAO} \cdot \cos\left(\frac{2\pi t}{6} + P_{SAO}\right) \\ + A_{AO} \cdot \cos\left(\frac{2\pi t}{12} + P_{AO}\right) + A_{QBO} \cdot \cos\left(\frac{2\pi t}{27.5} + P_{QBO}\right)$$

$$[O]_{Column} = \text{baseline} + A_{solar} \cdot I_{solar}(t + \text{shift}) + A_{SAO} \cdot \cos\left(\frac{2\pi t}{6} + P_{SAO}\right) \\ + A_{AO} \cdot \cos\left(\frac{2\pi t}{12} + P_{AO}\right) + A_{QBO} \cdot \cos\left(\frac{2\pi t}{27.5} + P_{QBO}\right) \quad (1)$$

- 5 The variable t represents the month since 2002 and the column density is fitted by amplitudes (A , atoms cm^{-3}) and phase shifts (P , months) of SAO (period of 6 months), AO (period of 12 months), and QBO (period of 27.5 months), complemented by the amplitude (A_{solar} , atoms cm^{-3} sfu^{-1}) and shift of the 11-year solar cycle effect, as well as an offset a baseline. The coefficient I_{solar} is the solar radio flux proxy ($F_{10.7}$ cm, in unit of sfu) taken from Tapping (2013). Typical mesospheric QBO

(MQBO) period is ~~reported approximately about~~ 27.5 months by investigating mesospheric zonal wind measurements (Ratnam et al., 2008; de Wit et al., 2013; Malhotra et al., 2016), ~~therefore a period of 27.5 months is considered for the QBO component in this analysis.~~ The baseline is given as the averaged value of the monthly mean column densities along the time series. The non-linear least squares fitting method (Levenberg–Marquardt algorithm) is applied to derive these fitting parameters, as described in detail by Kaufmann et al. (2013) and Zhu et al. (2015).

In Figure 10, the raw data and the fitting results are illustrated ~~, along with the linear fitting, considering only the first two components in in the upper panel.~~ Besides, the equation baseline plus the solar terms are also shown in the plot. The SolarMin and SolarMax values denote the fitted atomic oxygen column densities solely from the solar cycle component, under the solar minimum and solar maximum conditions, respectively. The SAO and AO components from the harmonic fitting are given in the middle and lower panel respectively. The [O] longtime variations are well characterized by the fit. The 11-year solar cycle effect is captured, in which the atomic oxygen density is ~~17.1~~ 17% smaller in 2008/2009 (minimum of solar cycle 23/24) than in 2002 ~~/2011~~ (near solar maximum conditions of solar cycles 23&24), due to different radiative forcing conditions during the solar cycles. ~~The atomic oxygen abundance difference of 17.1% under solar min/max conditions.~~ This agrees with model investigations and experimental results, which are normally in a range of around 10% to 30% (Schmidt et al., 2006; Marsh et al., 2007; Kaufmann et al., 2014; Zhu et al., 2015). A significant semiannual oscillation is observed, reaching a maximum in equinox seasons, which is in agreement with the analysis above for Figure 9, and the amplitude is about 18% (with respect to the baseline). The annual oscillation has an amplitude of ~~9.6~~ 10%, with the maximum being reached near summer solstices and the minimum near winter solstices. These results are consistent with the analyses of Zhu et al. (2015) and Lednyts'kyi et al. (2017), which reported SAO amplitudes on the order of 15% and 12%, AO amplitude of 11% and 7%, respectively. The QBO amplitude is ~~in on~~ the order of ~~1.7~~ 2%. The multiple linear fitting analyses on other latitudinal bands and altitudes also show a similar solar cycle effect as well as AO and SAO variations, as some examples are summarized in Table 2.

Table 2. Summary of multiple linear regression analysis results of monthly mean atomic oxygen column densities integrated over 80–97 km for 20° – 30° - N°N , 0° – 10° - N°N , and 30° – 20° - S°S from 2002 to 2011. The quantities are in unit of 10^{12} atoms cm^{-3} . A_{SAO} , A_{AO} , and A_{QBO} are the amplitudes of SAO, AO, and QBO, respectively.

Latitude bin	Offset <u>Baseline</u>	Solar Max	Solar Min	A_{SAO}	A_{AO}	A_{QBO}
20° – 30° - N°N	1.276	0.151	-0.067	0.23	0.122	0.022
0° – 10° - N°N	1.221	0.085	-0.044	0.272	0.126	0.05
30° – 20° - S°S	1.126	0.097	-0.052	0.183	0.074	0.025

It could be considered to add an additional slope term in the harmonic fitting (Equation 1) as well. In that case, the agreement between measurements and the fit increases marginally by about 2% with an additional slope term. But the fitting parameters are not independent any longer, because a strong correlation between the slope, the baseline and the solar terms are found, which was not the case before. This indicates that the inversion problem (to obtain the fitting parameters) is now under-determined. As an alternative approach, the solar ($F_{10.7}$) fitting parameter could be replaced by the slope term. In this

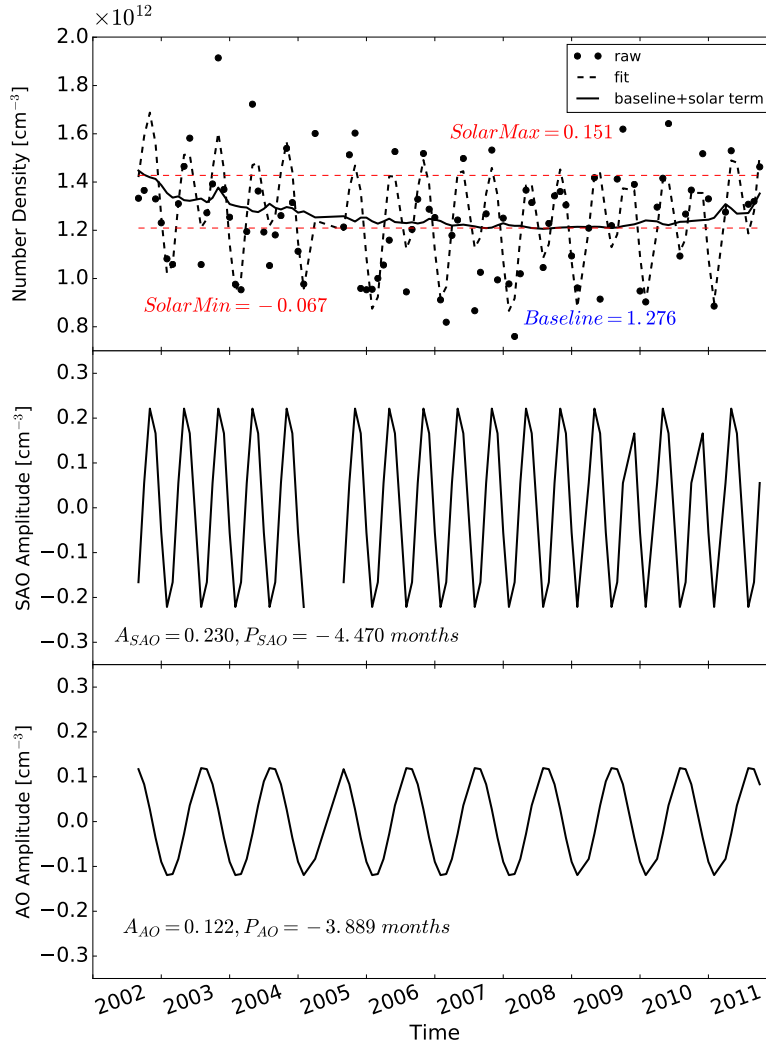


Figure 10. Multiple linear regression analysis of vertically integrated, monthly mean atomic oxygen densities of 80–97 km for 20° – 30° $N^{\circ}N$ from 2002 to 2011. (upper panel) The raw and fitted data are shown along with the linear fit, which represents the constant offset baseline plus the linear solar flux component components in the multiple linear regression results. The SolarMin and SolarMax values denote the fitted atomic oxygen column densities solely from the solar cycle component, under the solar minimum and solar maximum conditions respectively. (middle) SAO and (lower) AO parts are also illustrated with corresponding parameters. A_{SAO} , P_{SAO} , A_{AO} , and P_{AO} are the amplitudes and phase shifts of SAO and AO, respectively. The quantities of SolarMin, SolarMax, Offset baseline and amplitudes are in unit of 10^{12} atoms cm^{-3} . The phase shifts are in unit of months. The gap present in the SAO is caused by the data discontinuity.

case, the residual increases by about 5% and the fitting parameters are not correlated (except for the offset and slope terms). From a mathematical point of view, this is an alternative to the original fit (with solar, but without slope terms). For this setup, the slope is $-0.0002 \times 10^{12} \text{ cm}^{-3} \text{ month}^{-1}$, which means that there is virtually no trend apparent in the data. This can be

explained, if the change over time is considered as a combination of two linear trends, with a negative slope in the declining phase of the solar cycle and a positive slope in the following inclining phase. This hypothesis can be underpinned by looking at a subset of the time series, covering the time period from 2002 to 2009, only (roughly solar maximum to solar minimum). The slope for this period is about -3% per year, indicating a linear decrease of atomic oxygen by 21% for the given period.

5 If the $F_{10.7}$ dependency is considered instead, a similar drop is modeled, if a solar term with an amplitude of $0.0025 \times 10^{12} \text{ cm}^{-3} \text{ sfu}^{-1}$ is used. This value is similar to $0.002 \times 10^{12} \text{ cm}^{-3} \text{ sfu}^{-1}$, which is the value obtained when the total time series is considered. This line of arguments indicates that there is more likely a solar $F_{10.7}$ dependency apparent in the data than a plain linear dependency.

5 Discussion

10 5.1 ~~Validation by Comparison with~~ SCIAMACHY Data

The SCIAMACHY instrument, another limb sounder on board the Envisat satellite, observed OH emissions at various wavelengths from visible to infrared emissions (Bovensmann et al., 1999; Kaufmann et al., 2008). This provides us with the best opportunity for a comprehensive joint investigation of the GOMOS [O] dataset, as SCIAMACHY covers exactly the same OH(8–4) band wavelengths as GOMOS. Two more datasets of [O] derived from SCIAMACHY green line emissions

15 ([Kaufmann et al., 2014](#); [Zhu et al., 2015](#)) and OH(9–6) band airglow ([Zhu and Kaufmann, 2018](#)) are currently available.

SCIAMACHY performed the OH airglow measurements in dark limb-viewing mode in the flight direction, with the recorded spectra always ~~at near~~ a local solar time of 10 p.m. and a fixed altitude grid of 3.3 km. The OH(8–4) band observation is located in Channel 5 with a spectral resolution of 0.54 nm. SCIAMACHY data Version 8–2016 is adopted in this work. A continuous observation was performed during the entire lifetime of Envisat. The number of recorded profiles in one sample bin was around

20 100–300 before 2005 and significantly increased to 400–600 because of a change in instrument operations. SNRs of single profiles are normally on the order of 6 at peak altitudes and decrease to 1 at lower altitudes. After monthly zonal averaging, SNRs increase by one order of magnitude, and the mean noise level is around $0.6 \times 10^9 \text{ photons s}^{-1} \text{ cm}^{-2} \text{ nm}^{-1} \text{ sr}^{-1}$.

Theoretically, the SCIAMACHY and GOMOS measurements should be identical in the same wavelength range ~~of OH airglow emissions~~. In practice, however, due to effects of various factors, such as instrument characteristics ~~and radiometric~~

25 ~~calibration-, radiometric calibration and fields-of-view~~, they do not fully conform with each other in terms of absolute radiance or instrument line shapes. In this study, the two data products are found to be consistent in terms of absolute radiance within $\pm 20\%$ in the peak emissions layer (shown in Figure 11), after monthly zonal averaging. Particularly, the difference of the GOMOS data to the SCIAMACHY data is gradually becoming positive from negative over time, and the potential source for the drift could be a degradation of the GOMOS or SCIAMACHY instruments (Bramstedt et al., 2009), which is not fully

30 corrected or over-compensated in the level-0 calibration, and the change of the system sensitivities over time. One specific example of spectra comparison is given in Figure 12. The emission radiances from two data products are similar, but the GOMOS spectra are more noisy. ~~The atomic oxygen abundances derived from this example bin is given in Figure 15 (b)-~~

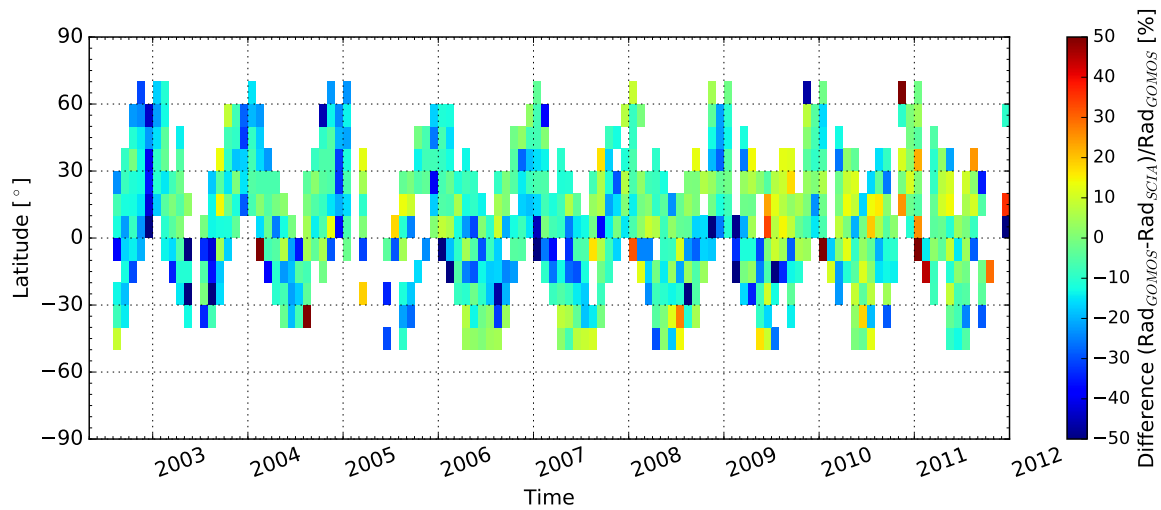


Figure 11. Temporal evolution of radiance differences (in percentage) between GOMOS and SCIAMACHY at an a tangent altitude of 86.5 km. The radiance is integrated over the wavelength of 930–935 nm. Negative numbers indicate that SCIAMACHY radiances are larger than those of GOMOS.

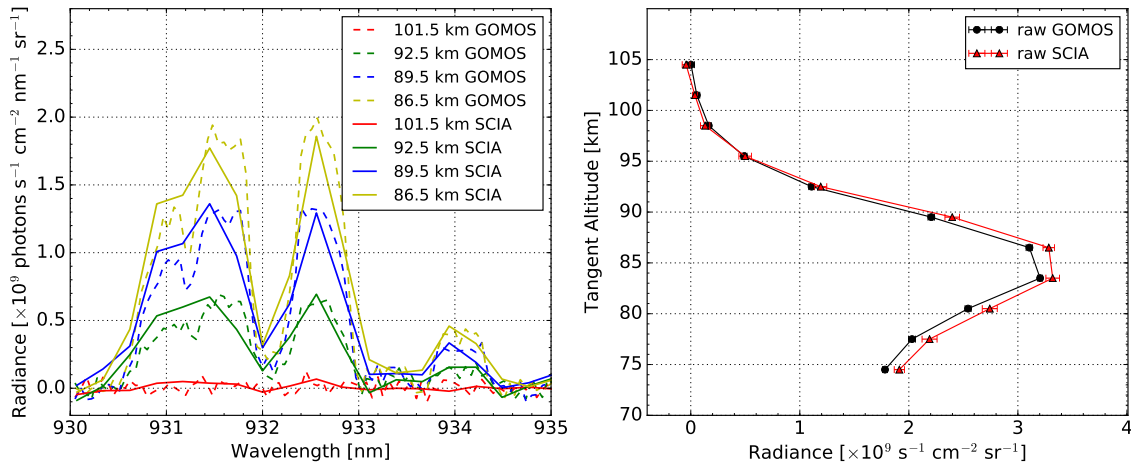


Figure 12. (leftLeft) SCIAMACHY (solid line) and GOMOS (dashed line) observations of monthly zonal mean OH(8–4) airglow emissions at the tangent altitudes, as given in the Figure legend for Apr. 2004 at 20°–30°N°N and a local time of 10–12 p.m. (rightRight) The spectrally integrated radiance over 930–935 nm versus tangent altitude for the same conditions. The error bars are measurement noise, computed as in Figure 4.

Comparison of monthly zonal mean atomic oxygen densities derived from hydroxyl airglow emissions observed by the GOMOS and SCIAMACHY instruments in various latitude bins for different months. SCIA-OH(9–6) represents the atomic

oxygen-dataset derived from the SCIAMACHY OH(9–6) band by Zhu and Kaufmann (2018); SCIA-OH(8–4) is the dataset from the SCIAMACHY OH(8–4) band; and GOMOS-OH(8–4) is from the GOMOS measurements of the OH(8–4) band.

The same retrieval procedure is applied to the SCIAMACHY data. The differences between the atomic oxygen abundances from the two instruments are illustrated in Figure 13. There are no major systematic discrepancies and they agree within a \pm 20% difference in most latitude-altitude bins as expected from the differences of the corresponding radiances. The GOMOS data is found to be over 20% lower in the northern hemisphere in February, and also in tropical regions in March, May, and September. GOMOS values appear to be 20% larger at low altitudes of around 80 km in some scattered bins. In general, these two atomic oxygen datasets derived from OH(8–4) airglow emissions ~~are consistent~~ agree with each other within the combined uncertainties in the context of absolute abundances.

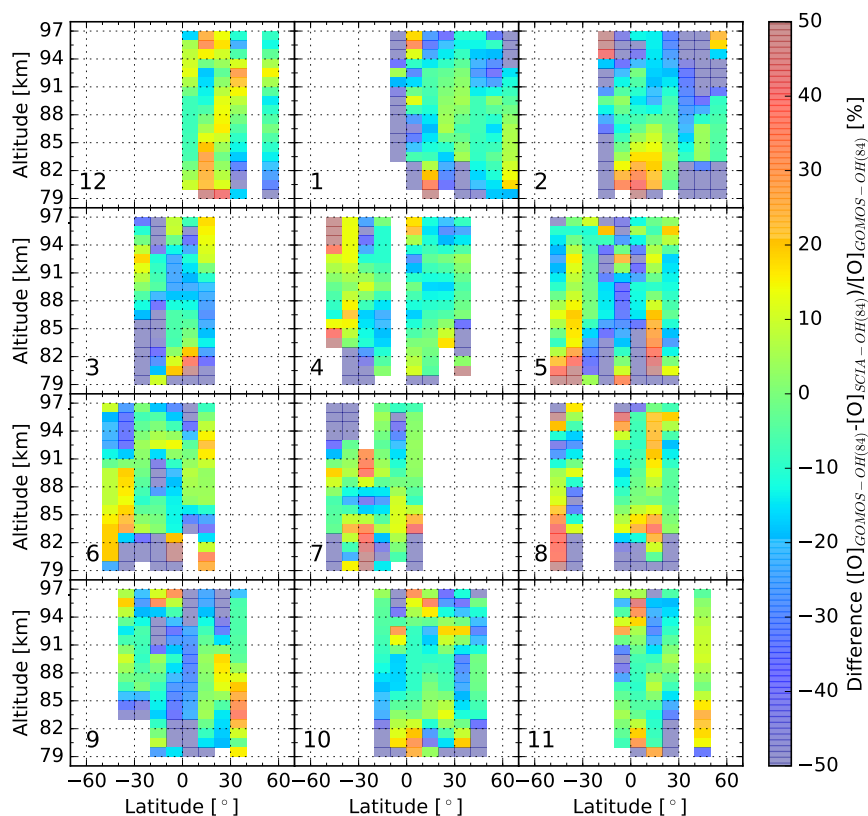


Figure 13. Latitude-altitude distribution of percentage differences between zonal mean atomic oxygen densities derived from GOMOS and SCIAMACHY OH(8–4) airglow emissions for 2007. Each row represents approximately a season. Negative numbers indicate that SCIAMACHY abundances are larger than those obtained from GOMOS. The data are linearly interpolated into a 1 km altitude grid. The numbers in the subplots indicate the month of the year.

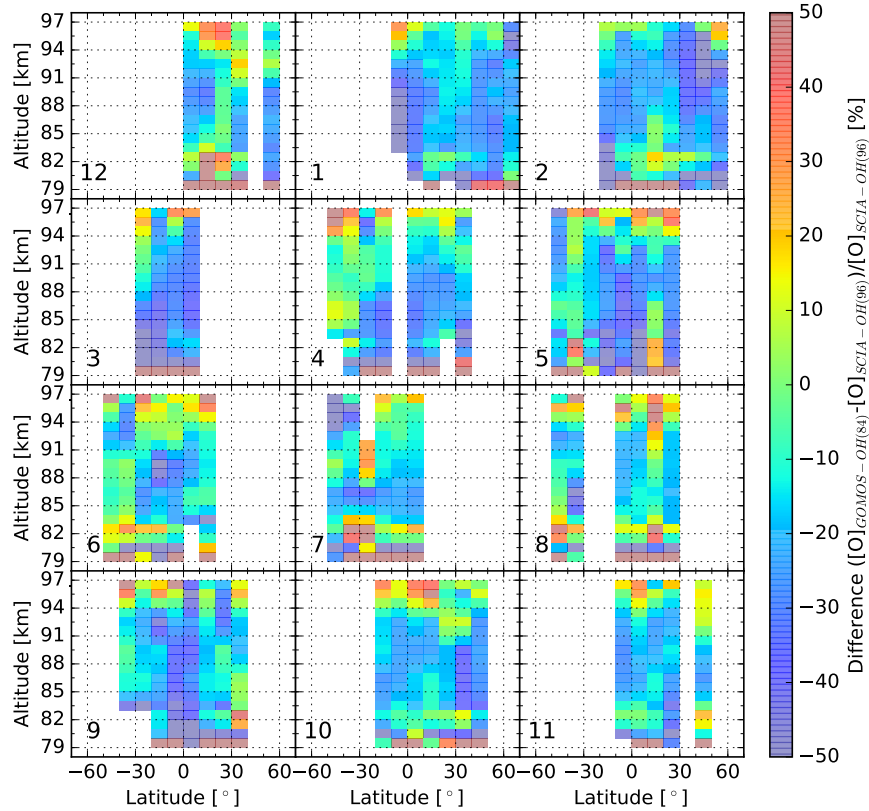


Figure 14. Latitude-altitude distribution of percentage differences between zonal mean atomic oxygen densities derived from GOMOS OH(8–4) and SCIAMACHY OH(9–6) airglow emissions for 2007. The SCIAMACHY OH(9–6) are taken from Zhu and Kaufmann (2018). This figure is plotted in a way similar to Figure 13. Negative numbers indicate that SCIAMACHY OH(9–6) atomic oxygen abundances are larger than the GOMOS OH(8–4) abundances.

5 **A** Similarly, a latitude-altitude comparison of the GOMOS data with atomic oxygen obtained from SCIAMACHY-SCIAMACHY OH(9–6) emissions (Zhu and Kaufmann, 2018) is given in Figure 14 for 2007. In general, these two dataset agree with each other, but the GOMOS OH(8–4) dataset is found to be around 10–20% lower than the SCIAMACHY OH(9–6) dataset in most latitude bins, especially in the altitude region of 85–95 km. The difference between the two datasets becomes more than 20% at some data points near the equator in March, May and September. Combining the derived results from SCIAMACHY OH(8–4), an inter-comparison of the three datasets is given in Figure 15 for different latitudinal and seasonal conditions. The absolute abundances of the three datasets are in the same order of magnitude and they agree with each other at the altitude region of interest of 80–95 km. Specifically, atomic oxygen abundances derived from OH($\nu=88-4$) emissions by both instruments are found to be around 10–20% lower than those derived from OH($\nu=99-6$) at around 90 km. This might be explained by a

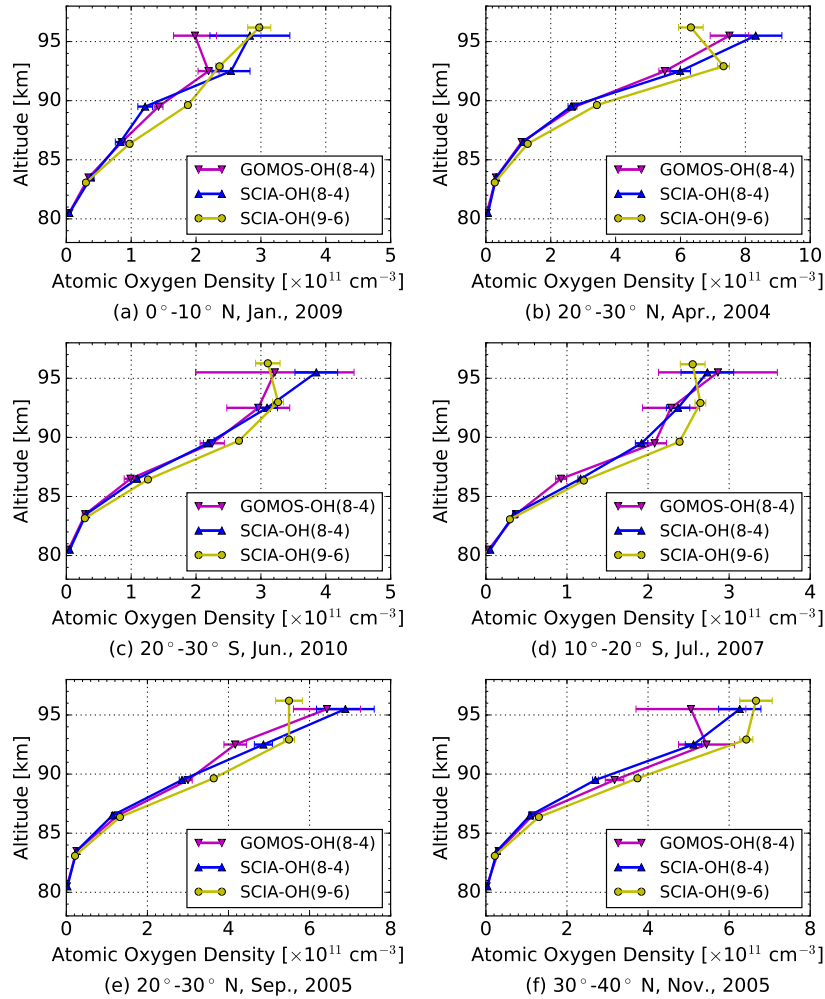


Figure 15. Comparison of monthly zonal mean atomic oxygen densities derived from hydroxyl airglow emissions observed by the GOMOS and SCIAMACHY instruments in various latitude bins for different months. SCIA-OH(9-6) represents the atomic oxygen dataset derived from the SCIAMACHY OH(9-6) band by Zhu and Kaufmann (2018); SCIA-OH(8-4) is the dataset from the SCIAMACHY OH(8-4) band; and GOMOS-OH(8-4) is from the GOMOS measurements of the OH(8-4) band.

slight underestimation of the quenching of OH($v=9$) to OH($v=8$) by O₂, an overestimation of the deactivation of OH($v=8$) due to collisions with atomic or molecular oxygen, or the over/under-estimation of the branching factors f_9 and f_8 in the OH airglow model.

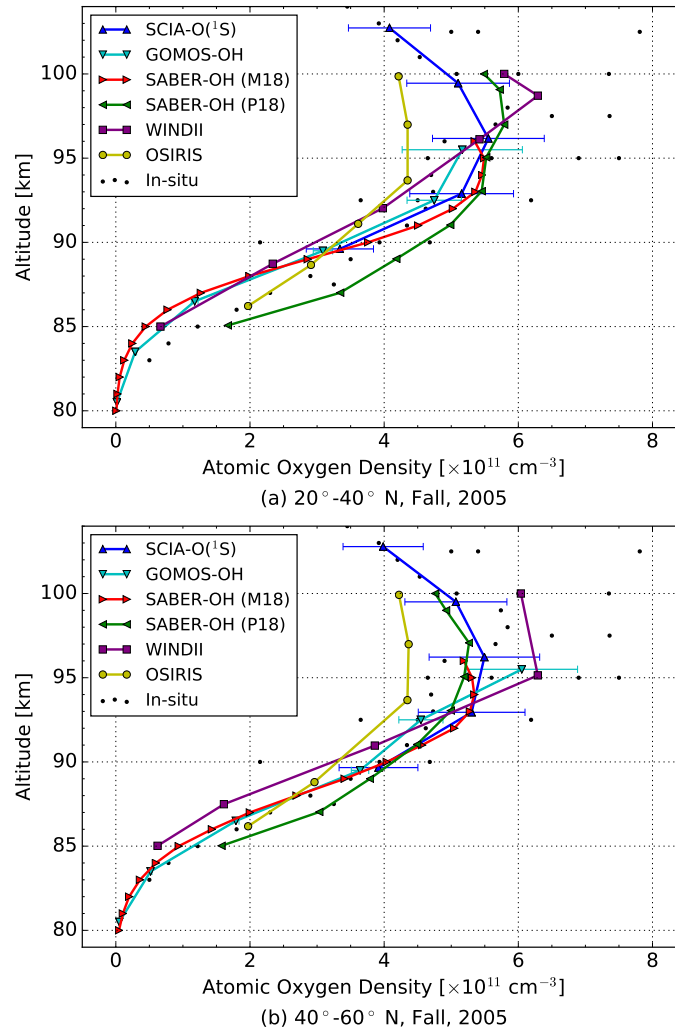


Figure 16. Comparison of derived atomic oxygen densities derived from various instruments and measurement techniques averaged for 20°-40°N (a) and 40°-60°N (b) in autumn (Sep., Oct., Nov.), 2005. SCIA-O(¹S) is the atomic oxygen data derived from SCIAMACHY green line emissions (Kaufmann et al., 2014; Zhu et al., 2015); SABER-OH refers to the atomic oxygen datasets derived by Mlynczak et al. (2018) (M18); and Panka et al. (2018) (P18) from SABER hydroxyl airglow emissions. The WINDII dataset is obtained from WINDII combined hydroxyl and green line observations, 1993 (Russell and Lowe, 2003; Russell et al., 2005), while the OSIRIS dataset is derived from OSIRIS O₂ A band measurements (Sheese et al., 2011). In situ data are obtained from rocket-borne experiments with mass spectrometers, conducted at different local times at 37-40°N, from 1972 to 1976 (Offermann and Grossmann, 1973; Trinks et al., 1978; Offermann et al., 1981).

5.2 Comparison with Other Datasets

There are a number of O₂ and O excited [statesstate emissions](#), which can also be used [as proxies for to derive](#) atomic oxygen. This includes O(¹S) green line and O₂ A-band emissions. Their modeling is mostly independent from the calculation of OH(ν) emissions, although some processes have to be considered in all models. Rocket-borne in situ measurements of atomic oxygen are the most independent from methods based on nightglow. Mostly performed in the 1970s ([Offermann et al., 1981](#)) (e.g. [Dickinson et al., 1980](#); [Sharp, 1980](#); [Offermann et al., 1981](#)), the measurements are very rare and selective [in terms of the local time and location](#). Figure 16 gives an impression of how the various datasets of atomic oxygen available in the literature fit to each other. All the sets are selected using a similar local time of around 10–11 p.m., with the exception of OSIRIS (6:30 p.m.) and in situ data with diverse local times at midnight or in the afternoon.

The datasets agree within their combined uncertainties in most cases. The absolute abundances are typically $4\text{--}6 \times 10^{11}$ atoms cm⁻³ above 90 km and decrease with descending altitudes by one order of magnitude (at around 80 km) for mid-latitude in autumn. GOMOS data are around 10% lower than SCIAMACHY-O(¹S) and both SABER-OH datasets at 90–95 km, but remain in good agreement with these datasets at lower altitudes below 90 km. The OSIRIS dataset appears as the lower bound of the values above 90 km, as it is always the lowest in this region, while it becomes relatively large below 90 km. The WINDII dataset is around 10% lower than the GOMOS-OH data at an altitude of 87–92 km, but they generally fit to each other. In situ data scatter in a large variation, which might be caused by the diurnal tides (local time differences), and the GOMOS-OH dataset is still located in its overall range of spread.

6 Conclusions

GOMOS limb observations of the background atmosphere provide the opportunity to retrieve atomic oxygen abundances from hydroxyl nightglow emissions at the mesopause. A global night-time [O] dataset is obtained by applying the OH modeling and retrieval method to the monthly zonal mean of GOMOS limb measurements, [with the atmospheric background profiles of temperature, total density and ozone taken from the SABER measurements](#). Its uncertainty comes from the measurement noise (around 5%), selected relaxation schemes and kinetic parameters in OH modeling (contributing around 20% in total) and background atmosphere inputs, for example atmospheric temperature, ozone (around 5% to 20%). The obtained profiles present an overall picture of the vertical distribution of atomic oxygen from 80 km to 100 km. A temporal analysis of the profiles shows 11-year solar cycle effect tendencies as well as semiannual and annual variations, of which SAO is the most prominent.

The GOMOS data agrees with the SCIAMACHY OH(8–4) measurements, with deviations typically smaller than 20%. They are, on average, about ~~10~~ [10–20%](#) lower than atomic oxygen data obtained from SCIAMACHY OH(9–6) observations. This might indicate that the collisional energy exchange between OH($\nu=9$) and OH($\nu=8$) via collisions with O₂ and O in the OH airglow model requires some readjustments. [Compared to other datasets derived from various instrument measurements, such as SABER, WINDII, OSIRIS and in situ rocket experiments, the GOMOS data also demonstrates an agreement with these datasets within their combined uncertainties.](#)

Data availability. The GOMOS and SCIAMACHY data used in this study are available to the public at <ftp://eo-a-dp.eo.esa.int> as part of the Cat-1 project 2515. SABER Version 2.0 can be downloaded from <http://saber.gats-inc.com>. Derived atomic oxygen datasets are available on request.

Appendix A: Fitting of the selected collisional rate coefficients for OH(v=8)

- 5 Some rate coefficients used in this work are obtained by simultaneously fitting the OH airglow model to measured limb radiances of OH(9-6) and OH(8-5) bands. The measurements are taken from SCIAMACHY channel 6 radiances. The OH(9-6) band radiance is integrated over the wavelength range of 1378-1404 nm, and the OH(8-5) band is integrated over 1297-1326 nm. The selected parameters are adjusted in such a way that the ratio between the simulated radiances of the two bands is consistent with the ratio obtained from the measurements. Several cases with different rate coefficients or combinations being
- 10 adjusted in the fitting are considered, as given in the Table A1. The fitting results of different cases are illustrated in the Figure A1, as compared to the SCIAMACHY measurements. Model simulations of cases b, c and d give a good agreement with the measurements. The rate coefficient for the collisional removal of OH(v=8) by atomic oxygen differs by nearly one order of magnitude from literature (Xu et al., 2012), and the fitted parameters should agree with the laboratory measurements within the combined uncertainties if available (Dyer et al., 1997). Therefore the case b is chosen and applied in this work. The
- 15 utilization of cases c and d will influence the retrieval results, that atomic oxygen abundances will differ by around 5% above 90 km and 15% at 80 km compared to case b.

Table A1. The comparison of study cases with the applied rate coefficients being summarized. The adjusted parameters and their fitted values are marked bold, while the coefficients taken from laboratory measurements are underlined and marked italic.

<u>Study case</u>	<u>$k_{O(s)} \times 10^{-10} \text{ cm}^3 \text{ s}^{-1}$</u>	<u>$k_{O_2(s)} \times 10^{-12} \text{ cm}^3 \text{ s}^{-1}$</u>	<u>$k_{N_2(s)} \times 10^{-13} \text{ cm}^3 \text{ s}^{-1}$</u>	<u>$k_{O_2(9,s)} \times 10^{-13} \text{ cm}^3 \text{ s}^{-1}$</u>
<u>a</u>	<u>1.2</u>	<u>8.0</u>	<u>7.0</u>	<u>42.0</u>
<u>b</u>	0.65	<u>8.0</u>	<u>7.0</u>	8.9
<u>c</u>	0.25	12.0	<u>7.0</u>	<u>42.0</u>
<u>d</u>	0.35	<u>8.0</u>	15.0	<u>42.0</u>
<u>e</u>	<u>2.0</u>	5.5	<u>7.0</u>	<u>42.0</u>
<u>f</u>	<u>2.0</u>	<u>8.0</u>	4.5	<u>42.0</u>

Author contributions. QC processed the data, performed the analysis and drafted the manuscript. MK and YZ initiated the topic, provided insight and instructions, and discussed the results regularly. All authors contributed to the revision and improvement of the paper.

Competing interests. The authors declare that they have no conflict of interest.

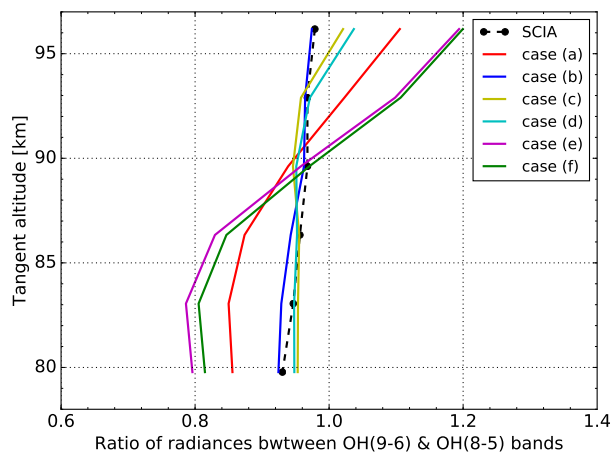


Figure A1. The ratio of the integrated limb radiances between the OH(9–6) (1378–1404 nm) and OH(8–5) (1297–1326 nm) bands versus tangent altitude. The raw data (black dashed line) is taken from the SCIAMACHY channel 6 measurements. The fitted results (solid line) are obtained by applying the rate coefficients with respect to different cases.

Acknowledgements. Q. Chen was supported in her work by the China Scholarship Council. The work of Y. Zhu was supported by the 2017 Helmholtz–OCPC Programme and the International Postdoctoral Exchange Fellowship Program 2017. We also thank three anonymous referees for their valuable comments and suggestions.

References

- Adler-Golden, S.: Kinetic parameters for OH nightglow modeling consistent with recent laboratory measurements, *Journal of Geophysical Research: Space Physics*, 102, 19 969–19 976, <https://doi.org/10.1029/97JA01622>, <https://agupubs.onlinelibrary.wiley.com/doi/abs/10.1029/97JA01622>, 1997.
- 5 Baker, D., Pendleton Jr., W., Steed, A., Huppi, R., and Stair Jr., A. T.: Near-infrared spectrum of an aurora, *Geophysical Research Letters*, 82, 1601–1609, <https://doi.org/10.1029/JA082i010p01601>, <https://agupubs.onlinelibrary.wiley.com/doi/abs/10.1029/JA082i010p01601>, 1977.
- Barrot, G., Bertaux, J.-L., Fraisse, R., and Mangin, A.: GOMOS calibration on Envisat-status on December 2002, in: *Proc. of Envisat Validation Workshop*, 2003.
- 10 Bellisario, C., Keckhut, P., Blanot, L., Hauchecorne, A., and Simoneau, P.: O₂ and OH night airglow emission derived from GOMOS-Envisat instrument, *Journal of Atmospheric and Oceanic Technology*, 31, 1301–1311, <https://doi.org/10.1175/JTECH-D-13-00135.1>, <https://hal.archives-ouvertes.fr/hal-00968748>, 2014.
- Bovensmann, H., Burrows, J. P., Buchwitz, M., Frerick, J., Noël, S., Rozanov, V. V., Chance, K. V., and Goede, A. P. H.: SCIAMACHY: Mission objectives and measurement modes, *Journal of the Atmospheric Sciences*, 56, 127–150, [https://doi.org/10.1175/1520-0469\(1999\)056<0127:SMOAMM>2.0.CO;2](https://doi.org/10.1175/1520-0469(1999)056<0127:SMOAMM>2.0.CO;2), 1999.
- 15 Bramstedt, K., Noël, S., Bovensmann, H., Burrows, J. P., Lerot, C., Tilstra, L., Lichtenberg, G., Dehn, A., and Fehr, T.: SCIAMACHY monitoring factors: Observation and end-to-end correction of instrument performance degradation, 2009.
- Brasseur, G. and Offermann, D.: Recombination of atomic oxygen near the mesopause: Interpretation of rocket data, *Journal of Geophysical Research: Atmospheres*, 91, 10 818–10 824, <https://doi.org/10.1029/JD091iD10p10818>, <https://agupubs.onlinelibrary.wiley.com/doi/abs/10.1029/JD091iD10p10818>, 1986.
- 20 Brasseur, G. P. and Solomon, S.: *Aeronomy of the middle atmosphere: Chemistry and physics of the stratosphere and mesosphere*, vol. 32 of *Atmospheric and Oceanographic Sciences Library*, Springer Netherlands, 3 edn., 2005.
- Cosby, P. C. and Slinger, T. G.: OH spectroscopy and chemistry investigated with astronomical sky spectra, *Canadian Journal of Physics*, 85, 77–99, <https://doi.org/10.1139/p06-088>, <https://doi.org/10.1139/p06-088>, 2007.
- 25 Dawkins, E. C. M., Feofilov, A., Rezac, L., Kutepov, A. A., Janches, D., Höffner, J., Chu, X., Lu, X., Mlynczak, M. G., and Russell III, J.: Validation of SABER v2.0 operational temperature data with ground-based lidars in the Mesosphere-Lower Thermosphere Region (75-105 km), *Journal of Geophysical Research: Atmospheres*, 123, 9916–9934, <https://doi.org/10.1029/2018JD028742>, <https://agupubs.onlinelibrary.wiley.com/doi/abs/10.1029/2018JD028742>, 2018.
- de Wit, R. J., Hibbins, R. E., Espy, P. J., and Mitchell, N. J.: Interannual variability of mesopause zonal winds over Ascension Island: Coupling to the stratospheric QBO, *Journal of Geophysical Research: Atmospheres*, 118, 12,052–12,060, <https://doi.org/10.1002/2013JD020203>, <https://agupubs.onlinelibrary.wiley.com/doi/abs/10.1002/2013JD020203>, 2013.
- 30 Dehn, A.: Quality readme file for GOMOS level 1b data version GOMOS/6.01, Tech. Rep. ENVI-GSOP-EOGD-QD-12-0116, European Space Agency, 2012.
- Dickinson, P. H. G., Bolden, R. C., and Young, R. A.: Measurement of atomic oxygen in the lower ionosphere using a rocket-borne resonance lamp, *Nature*, 252, pages 289–291, <https://doi.org/https://doi.org/10.1038/252289a0>, 1974.
- 35

- Dickinson, P. H. G., Bain, W. C., Thomas, L., Williams, E. R., Jenkins, D. B., and Twiddy, N. D.: The determination of the atomic oxygen concentration and associated parameters in the lower ionosphere, *Proceedings of the Royal Society of London. Series A, Mathematical and Physical Sciences*, 369, 379–408, <http://www.jstor.org/stable/2398309>, 1980.
- Dyer, M. J., Knutsen, K., and Copeland, R. A.: Energy transfer in the ground state of OH: Measurements of OH($\nu=8,10,11$) removal, *The Journal of Chemical Physics*, 107, 7809–7815, <https://doi.org/10.1063/1.475094>, 1997.
- ESA: European space agency-Envisat GOMOS Product Handbook, <http://envisat.esa.int/handbooks/gomos/CNTR.html>, [Online; accessed 8-November-2016], 2010.
- Fytterer, T., von Savigny, C., Mlynczak, M., and Sinnhuber, M.: Model results of OH airglow considering four different wavelength regions to derive night-time atomic oxygen and atomic hydrogen in the mesopause region, *Atmospheric Chemistry and Physics*, 19, 1835–1851, <https://doi.org/10.5194/acp-19-1835-2019>, <https://www.atmos-chem-phys.net/19/1835/2019/>, 2019.
- Gao, H., Nee, J.-B., and Xu, J.: The emission of oxygen green line and density of O atom determined by using ISUAL and SABER measurements, *Annales Geophysicae*, 30, 695–701, <https://doi.org/10.5194/angeo-30-695-2012>, <https://www.ann-geophys.net/30/695/2012/>, 2012.
- Gottwald, M., Diekmann, F.-J., and Diekmann, F.-J.: ENVISAT - SCIAMACHY's Host, in: SCIAMACHY - Exploring the Changing Earth's Atmosphere, XVI, 225, Springer Netherlands, <https://doi.org/10.1007/978-90-481-9896-2>, 2011.
- Hays, P. B., Abreu, V. J., Dobbs, M. E., Gell, D. A., Grassl, H. J., and Skinner, W. R.: The high-resolution doppler imager on the Upper Atmosphere Research Satellite, *Journal of Geophysical Research: Atmospheres*, 98, 10 713–10 723, <https://doi.org/10.1029/93JD00409>, <https://agupubs.onlinelibrary.wiley.com/doi/abs/10.1029/93JD00409>, 1993.
- Kalogerakis, K. S.: A previously unrecognized source of the O₂ Atmospheric band emission in Earth's nightglow, *Science Advances*, 5, <https://doi.org/10.1126/sciadv.aau9255>, <http://advances.sciencemag.org/content/5/3/eaau9255>, 2019.
- Kalogerakis, K. S., Smith, G. P., and Copeland, R. A.: Collisional removal of OH(X²Π, $\nu = 9$) by O, O₂, O₃, N₂, and CO₂, *Journal of Geophysical Research: Atmospheres*, 116, <https://doi.org/10.1029/2011JD015734>, <https://agupubs.onlinelibrary.wiley.com/doi/abs/10.1029/2011JD015734>, 2011.
- Kalogerakis, K. S., Matsiev, D., Sharma, R. D., and Wintersteiner, P. P.: Resolving the mesospheric nighttime 4.3 μm emission puzzle: Laboratory demonstration of new mechanism for OH(ν) relaxation, *Geophysical Research Letters*, 43, 8835–8843, <https://doi.org/10.1002/2016GL069645>, <https://agupubs.onlinelibrary.wiley.com/doi/abs/10.1002/2016GL069645>, 2016.
- Kaufmann, M., Lehmann, C., Hoffmann, L., Funke, B., López-Puertas, M., Savigny, C., and Riese, M.: Chemical heating rates derived from SCIAMACHY vibrationally excited OH limb emission spectra, *Advances in Space Research*, 41, 1914 – 1920, <https://doi.org/https://doi.org/10.1016/j.asr.2007.07.045>, <http://www.sciencedirect.com/science/article/pii/S0273117707008459>, 2008.
- Kaufmann, M., Ern, M., Lehmann, C., and Riese, M.: The response of atomic hydrogen to solar radiation changes, in: *Climate And Weather of the Sun-Earth System (CAWSES): Highlights from a priority program*, pp. 171–188, Springer Atmospheric Sciences, <http://juser.fz-juelich.de/record/22385>, 2013.
- Kaufmann, M., Zhu, Y., Ern, M., and Riese, M.: Global distribution of atomic oxygen in the mesopause region as derived from SCIAMACHY O(¹S) green line measurements, *Geophysical Research Letters*, 41, 6274–6280, <https://doi.org/10.1002/2014GL060574>, <https://agupubs.onlinelibrary.wiley.com/doi/abs/10.1002/2014GL060574>, 2014.
- Kyrölä, E., Tamminen, J., Sofieva, V., Bertaux, J. L., Hauchecorne, A., Dalaudier, F., Fussen, D., Vanhellefont, F., Fanton d'Andon, O., Barrot, G., Guirlet, M., Mangin, A., Blanot, L., Fehr, T., Saavedra de Miguel, L., and Fraisse, R.: Retrieval of atmospheric parameters

- from GOMOS data, *Atmospheric Chemistry and Physics*, 10, 11 881–11 903, <https://doi.org/10.5194/acp-10-11881-2010>, <http://www.atmos-chem-phys.net/10/11881/2010/>, 2010.
- 5 Kyrölä, E., Blanot, L., Tamminen, J., Sofieva, V., Bertaux, J. L., Hauchecorne, A., Dalaudier, F., Fussen, D., Vanhellemont, F., d'Andon, O. F., and Barrot, G.: Algorithm theoretical basis document version 3.0, Tech. Rep. GOM-FMI-TN-040, Finnish Meteorological Institute and ACRI-ST and LATMOS-IPSL and Institut d'Aéronomie Spatiale de Belgique, 2012.
- Lacoursière, J., Dyer, M. J., and Copeland, R. A.: Temperature dependence of the collisional energy transfer of OH($v=10$) between 220 and 310 K, *The Journal of Chemical Physics*, 118, 1661–1666, <https://doi.org/10.1063/1.1530581>, <https://doi.org/10.1063/1.1530581>, 2003.
- Lednyts'kyy, O., von Savigny, C., Eichmann, K.-U., and Mlynczak, M. G.: Atomic oxygen retrievals in the MLT region from SCIAMACHY nightglow limb measurements, *Atmospheric Measurement Techniques*, 8, 1021–1041, <https://doi.org/10.5194/amt-8-1021-2015>, <https://www.atmos-meas-tech.net/8/1021/2015/>, 2015.
- 10 Lednyts'kyy, O., von Savigny, C., and Weber, M.: Sensitivity of equatorial atomic oxygen in the MLT region to the 11-year and 27-day solar cycles, *Journal of Atmospheric and Solar-Terrestrial Physics*, 162, 136 – 150, <https://doi.org/https://doi.org/10.1016/j.jastp.2016.11.003>, <http://www.sciencedirect.com/science/article/pii/S1364682616303911>, layered Phenomena in the Mesopause Region, 2017.
- Li, F., Liu, A. Z., and Swenson, G. R.: Characteristics of instabilities in the mesopause region over Maui, Hawaii, *Journal of Geophysical Research: Atmospheres*, 110, <https://doi.org/10.1029/2004JD005097>, <https://agupubs.onlinelibrary.wiley.com/doi/abs/10.1029/2004JD005097>, 2005.
- 15 Malhotra, G., Ruohoniemi, J. M., Baker, J. B. H., Hibbins, R. E., and McWilliams, K. A.: HF radar observations of a quasi-biennial oscillation in midlatitude mesospheric winds, *Journal of Geophysical Research: Atmospheres*, 121, 12,677–12,689, <https://doi.org/10.1002/2016JD024935>, <https://agupubs.onlinelibrary.wiley.com/doi/abs/10.1002/2016JD024935>, 2016.
- 20 Marsh, D. R., Garcia, R. R., Kinnison, D. E., Boville, B. A., Sassi, F., Solomon, S. C., and Matthes, K.: Modeling the whole atmosphere response to solar cycle changes in radiative and geomagnetic forcing, *Journal of Geophysical Research: Atmospheres*, 112, n/a–n/a, <https://doi.org/10.1029/2006JD008306>, <http://dx.doi.org/10.1029/2006JD008306>, d23306, 2007.
- Massimo Cardaci, R. and Lannone, Q.: ENVISAT-1 products specifications - Volume 10:GOMOS products specifications, Tech. Rep. PO-RS-MDA-GS-2009/IDEAS-SER-IPF-SPE-1124, Serco SpA, 2012.
- 25 Mlynczak, M. G., Hunt, L. A., Marshall, B. T., Mertens, C. J., Russell, J. M., Siskind, D., Thompson, R. E., and Gordley, L. L.: Radiative constraints on the minimum atomic oxygen concentration in the mesopause region, *Geophysical Research Letters*, 40, 3777–3780, <https://doi.org/10.1002/grl.50725>, <https://agupubs.onlinelibrary.wiley.com/doi/abs/10.1002/grl.50725>, 2013a.
- Mlynczak, M. G., Hunt, L. A., Mast, J. C., Thomas Marshall, B., Russell, J. M., Smith, A. K., Siskind, D. E., Yee, J.-H., Mertens, C. J., Javier Martin-Torres, F., Earl Thompson, R., Drob, D. P., and Gordley, L. L.: Atomic oxygen in the mesosphere and lower thermosphere derived from SABER: Algorithm theoretical basis and measurement uncertainty, *Journal of Geophysical Research: Atmospheres*, 118, 5724–5735, <https://doi.org/10.1002/jgrd.50401>, <https://agupubs.onlinelibrary.wiley.com/doi/abs/10.1002/jgrd.50401>, 2013b.
- 30 Mlynczak, M. G., Hunt, L. H., Mertens, C. J., Marshall, B. T., Russell, J. M., López Puertas, M., Smith, A. K., Siskind, D. E., Mast, J. C., Thompson, R. E., and Gordley, L. L.: Radiative and energetic constraints on the global annual mean atomic oxygen concentration in the mesopause region, *Journal of Geophysical Research: Atmospheres*, 118, 5796–5802, <https://doi.org/10.1002/jgrd.50400>, <https://agupubs.onlinelibrary.wiley.com/doi/abs/10.1002/jgrd.50400>, 2013c.
- 35 Mlynczak, M. G., Hunt, L. A., Russell, J. M., and Marshall, B. T.: Updated SABER night atomic oxygen and implications for SABER ozone and atomic hydrogen, *Geophysical Research Letters*, 45, 5735–5741, <https://doi.org/10.1029/2018GL077377>, <https://agupubs.onlinelibrary.wiley.com/doi/abs/10.1029/2018GL077377>, 2018.

- Offermann, D. and Grossmann, K. U.: Thermospheric density and composition as determined by a mass spectrometer with cryo ion source, *Journal of Geophysical Research*, 78, 8296–8304, <https://doi.org/10.1029/JA078i034p08296>, <https://agupubs.onlinelibrary.wiley.com/doi/abs/10.1029/JA078i034p08296>, 1973.
- Offermann, D., Friedrich, V., Ross, P., and Zahn, U. V.: Neutral gas composition measurements between 80 and 120 km, *Planetary and Space Science*, 29, 747 – 764, [https://doi.org/https://doi.org/10.1016/0032-0633\(81\)90046-5](https://doi.org/https://doi.org/10.1016/0032-0633(81)90046-5), <http://www.sciencedirect.com/science/article/pii/0032063381900465>, 1981.
- Oliva, E., Origlia, L., Scuderi, S., Benatti, S., Carleo, I., Lapenna, E., Mucciarelli, A., Baffa, C., Biliotti, V., Carbonaro, L., Falcini, G., Giani, E., Iuzzolino, M., Massi, F., Sanna, N., Sozzi, M., Tozzi, A., Ghedina, A., Ghinassi, F., and Pedani, M.: Lines and continuum sky emission in the near infrared: Observational constraints from deep high spectral resolution spectra with GIANO-TNG, *Astronomy & Astrophysics*, 581, <https://doi.org/10.1051/0004-6361/201526291>, 2015.
- Panka, P. A., Kutepov, A. A., Kalogerakis, K. S., Janches, D., Russell, J. M., Rezac, L., Feofilov, A. G., Mlynczak, M. G., and Yiğit, E.: Resolving the mesospheric nighttime 4.3 μm emission puzzle: comparison of the $\text{CO}_2(\nu_3)$ and $\text{OH}(\nu)$ emission models, *Atmospheric Chemistry and Physics*, 17, 9751–9760, <https://doi.org/10.5194/acp-17-9751-2017>, <https://www.atmos-chem-phys.net/17/9751/2017/>, 2017.
- Panka, P. A., Kutepov, A. A., Rezac, L., Kalogerakis, K. S., Feofilov, A. G., Marsh, D., Janches, D., and Yiğit, E.: Atomic oxygen retrieved from the SABER 2.0- and 1.6- μm radiances using new first-principles nighttime $\text{OH}(\nu)$ model, *Geophysical Research Letters*, 45, 5798–5803, <https://doi.org/10.1029/2018GL077677>, <https://agupubs.onlinelibrary.wiley.com/doi/abs/10.1029/2018GL077677>, 2018.
- Picone, J. M., Hedin, A. E., Drob, D. P., and Aikin, A. C.: NRLMSISE-00 empirical model of the atmosphere: Statistical comparisons and scientific issues, *Journal of Geophysical Research: Space Physics*, 107, SIA 15–1–SIA 15–16, <https://doi.org/10.1029/2002JA009430>, <http://dx.doi.org/10.1029/2002JA009430>, 1468, 2002.
- Ratnam, M. V., Kumar, G. K., Murthy, B. V. K., Patra, A. K., Rao, V. V. M. J., Rao, S. V. B., Kumar, K. K., and Ramkumar, G.: Long-term variability of the low latitude mesospheric SAO and QBO and their relation with stratospheric QBO, *Geophysical Research Letters*, 35, <https://doi.org/10.1029/2008GL035390>, <https://agupubs.onlinelibrary.wiley.com/doi/abs/10.1029/2008GL035390>, 2008.
- Riese, M., Offermann, D., and Brasseur, G.: Energy released by recombination of atomic oxygen and related species at mesopause heights, *Journal of Geophysical Research: Atmospheres*, 99, 14 585–14 593, <https://doi.org/10.1029/94JD00356>, <https://agupubs.onlinelibrary.wiley.com/doi/abs/10.1029/94JD00356>, 1994.
- Rodgers, C. D.: *Inverse methods for atmospheric sounding: theory and practice*, World Scientific, 2000.
- Russell, J. P. and Lowe, R. P.: Atomic oxygen profiles (80–94 km) derived from Wind Imaging Interferometer/Upper Atmospheric Research Satellite measurements of the hydroxyl airglow: I. Validation of technique, *Journal of Geophysical Research: Atmospheres*, 108, 4662, <https://doi.org/10.1029/2003JD003454>, <https://agupubs.onlinelibrary.wiley.com/doi/abs/10.1029/2003JD003454>, 2003.
- Russell, J. P., Ward, W. E., Lowe, R. P., Roble, R. G., Shepherd, G. G., and Solheim, B.: Atomic oxygen profiles (80 to 115 km) derived from Wind Imaging Interferometer/Upper Atmospheric Research Satellite measurements of the hydroxyl and greenline airglow: Local time-latitude dependence, *Journal of Geophysical Research: Atmospheres*, 110, <https://doi.org/10.1029/2004JD005570>, <https://agupubs.onlinelibrary.wiley.com/doi/abs/10.1029/2004JD005570>, 2005.
- Sander, S., Abbatt, J., Barker, J., Burkholder, J., Friedl, R., Golden, D., Huie, R., Kurylo, M., Moortgat, G., Orkin, V., and Wine, P.: *Chemical kinetics and photochemical data for use in atmospheric studies, evaluation No. 17*, Tech. rep., Jet Propulsion Laboratory, California Institute of Technology, Pasadena, CA, 2011.

- Schmidt, H., Brasseur, G. P., Charron, M., Manzini, E., Giorgetta, M. A., Diehl, T., Fomichev, V. I., Kinnison, D., Marsh, D., and Walters, S.: The HAMMONIA chemistry climate model: Sensitivity of the mesopause region to the 11-Year solar cycle and CO₂ doubling, *Journal of Climate*, 19, 3903–3931, <https://doi.org/10.1175/JCLI3829.1>, <https://doi.org/10.1175/JCLI3829.1>, 2006.
- Sharma, R. D., Wintersteiner, P. P., and Kalogerakis, K. S.: A new mechanism for OH vibrational relaxation leading to enhanced CO₂ emissions in the nocturnal mesosphere, *Geophysical Research Letters*, 42, 4639–4647, <https://doi.org/10.1002/2015GL063724>, <https://doi.org/10.1002/2015GL063724>, 2015.
- Sharp, W. E.: Absolute concentrations of O(³P) in the lower thermosphere at night, *Geophysical Research Letters*, 7, 485–488, <https://doi.org/10.1029/GL007i007p00485>, <https://doi.org/10.1029/GL007i007p00485>, 1980.
- Sharp, W. E.: The measurement of atomic oxygen in the mesosphere and lower thermosphere, *Planetary and Space Science*, 39, 617–626, 1991.
- Sheese, P. E., McDade, I. C., Gattinger, R. L., and Llewellyn, E. J.: Atomic oxygen densities retrieved from Optical Spectrograph and Infrared Imaging System observations of O₂A-band airglow emission in the mesosphere and lower thermosphere, *Journal of Geophysical Research: Atmospheres*, 116, <https://doi.org/10.1029/2010JD014640>, <https://doi.org/10.1029/2010JD014640>, 2011.
- 15 Sheese, P. E., Llewellyn, E. J., Gattinger, R. L., and Strong, K.: OH Meinel band nightglow profiles from OSIRIS observations, *Journal of Geophysical Research: Atmospheres*, 119, 11,417–11,428, <https://doi.org/10.1002/2014JD021617>, <https://doi.org/10.1002/2014JD021617>, 2014.
- Smith, A. K., Marsh, D. R., Mlynczak, M. G., and Mast, J. C.: Temporal variations of atomic oxygen in the upper mesosphere from SABER, *Journal of Geophysical Research: Atmospheres*, 115, <https://doi.org/10.1029/2009JD013434>, <https://doi.org/10.1029/2009JD013434>, 2010.
- 20 Smith, S. A., Fritts, D. C., and Vanzandt, T. E.: Evidence for a saturated spectrum of atmospheric gravity waves, *Journal of the Atmospheric Sciences*, 44, 1404–1410, [https://doi.org/10.1175/1520-0469\(1987\)044<1404:EFASSO>2.0.CO;2](https://doi.org/10.1175/1520-0469(1987)044<1404:EFASSO>2.0.CO;2), [https://doi.org/10.1175/1520-0469\(1987\)044<1404:EFASSO>2.0.CO;2](https://doi.org/10.1175/1520-0469(1987)044<1404:EFASSO>2.0.CO;2), 1987.
- Swenson, G., Yee, Y., Vargas, F., and Liu, A.: Vertical diffusion transport of atomic oxygen in the mesopause region consistent with chemical losses and continuity: Global mean and inter-annual variability, *Journal of Atmospheric and Solar-Terrestrial Physics*, 178, 47–57, <https://doi.org/10.1016/j.jastp.2018.05.014>, <http://www.sciencedirect.com/science/article/pii/S1364682617305552>, 2018.
- 25 Tapping, K. F.: The 10.7cm solar radio flux (F10.7), *Space Weather*, 11, 394–406, <https://doi.org/10.1002/swe.20064>, <https://doi.org/10.1002/swe.20064>, 2013.
- Thomas, R. J.: Atomic hydrogen and atomic oxygen density in the mesopause region: Global and seasonal variations deduced from Solar Mesosphere Explorer near-infrared emissions, *Journal of Geophysical Research: Atmospheres*, 95, 16457–16476, <https://doi.org/10.1029/JD095iD10p16457>, <http://dx.doi.org/10.1029/JD095iD10p16457>, 1990.
- Tikhonov, A. and Arsenin, V.: Solutions of ill-posed problems, Scripta series in mathematics, Winston, <https://books.google.de/books?id=ECrvAAAAMAAJ>, 1977.
- Trinks, H., Offermann, D., von Zahn, U., and Steinhauer, C.: Neutral composition measurements between 90- and 220-km altitude by rocket-borne mass spectrometer, *Journal of Geophysical Research*, 83, 2169–2176, <https://doi.org/10.1029/JA083iA05p02169>, 1978.
- 35 van Gijssel, J. A. E., Swart, D. P. J., Baray, J.-L., Bencherif, H., Claude, H., Fehr, T., Godin-Beekmann, S., Hansen, G. H., Keckhut, P., Leblanc, T., McDermid, I. S., Meijer, Y. J., Nakane, H., Quel, E. J., Stebel, K., Steinbrecht, W., Strawbridge, K. B., Tatarov, B. I., and

- Wolfram, E. A.: GOMOS ozone profile validation using ground-based and balloon sonde measurements, *Atmospheric Chemistry and Physics*, 10, 10473–10488, <https://doi.org/10.5194/acp-10-10473-2010>, <http://www.atmos-chem-phys.net/10/10473/2010/>, 2010.
- Xu, J., Smith, A. K., Jiang, G., Gao, H., Wei, Y., Mlynchzak, M. G., and Russell III, J. M.: Strong longitudinal variations in the OH nightglow, *Geophysical Research Letters*, 37, <https://doi.org/10.1029/2010GL043972>, <https://agupubs.onlinelibrary.wiley.com/doi/abs/10.1029/2010GL043972>, 2010.
- 5 Xu, J., Gao, H., Smith, A. K., and Zhu, Y.: Using TIMED/SABER nightglow observations to investigate hydroxyl emission mechanisms in the mesopause region, *Journal of Geophysical Research: Atmospheres*, 117, n/a, <https://doi.org/10.1029/2011JD016342>, <https://agupubs.onlinelibrary.wiley.com/doi/abs/10.1029/2011JD016342>, 2012.
- Zhu, Y. and Kaufmann, M.: Atomic oxygen abundance retrieved from SCIAMACHY hydroxyl nightglow measurements, *Geophysical Research Letters*, 45, 9314–9322, <https://doi.org/10.1029/2018GL079259>, <https://agupubs.onlinelibrary.wiley.com/doi/abs/10.1029/2018GL079259>, 2018.
- 10 Zhu, Y., Kaufmann, M., Ern, M., and Riese, M.: Nighttime atomic oxygen in the mesopause region retrieved from SCIAMACHY O(¹S) green line measurements and its response to solar cycle variation, *Journal of Geophysical Research: Space Physics*, 120, 9057–9073, <https://doi.org/10.1002/2015JA021405>, <https://agupubs.onlinelibrary.wiley.com/doi/abs/10.1002/2015JA021405>, 2015.